Electronic Research Archive

https://www.aimspress.com/journal/era

ERA, 35(1): 100–133.
DOI: 10.3934/era.2027004
Received: 04 October 2026
Revised: 05 November 2026
Accepted: 17 November 2026
Published: 27 November 2026

Research article

Fear effects on equilibrium and sliding transitions in a two-threshold Filippov pest–natural-enemy model

Chenxi Wang, Dan Jin*and Ruizhi Yang

Department of Mathematics, Northeast Forestry University, Harbin 150040, China

* **Correspondence:** Email: jindan720@163.com.

Abstract: Threshold-based pest management produces discontinuous dynamics in which both pest density and natural-enemy abundance determine the active control regime. We investigated how fear induced by natural enemies affects equilibria and sliding transitions in a two-threshold Filippov pest–natural-enemy model incorporating a strong Allee effect. Two analytical reductions characterize the influence of fear. In the no-control and reduced-dose regimes, the Jacobian trace at a positive equilibrium admits a factorization whose numerator is independent of the fear intensity. Consequently, away from the degenerate case, varying fear does not change the local stability of these equilibria or induce a Hopf bifurcation within either smooth regime. In the pesticide-and-release regime, equilibrium existence, multiplicity, and determinant sign are characterized by a scalar level function. A Sturm sequence certifies exactly two equilibria for the baseline parameters, one stable and one saddle. Under the stated existence condition, these equilibria persist up to a unique terminal fear threshold, although the associated tangency need not be unique. On the horizontal switching manifold, the pseudo-equilibrium moves monotonically under suitable conditions and undergoes a boundary-equilibrium collision with the reduced-dose equilibrium. Numerical simulations support the analytical thresholds and illustrate distinct terminal outcomes without establishing global basins. These results show that fear can reshape equilibrium admissibility and sliding dynamics even when smooth local stability remains unchanged. The fear factor also slows negative growth below the Allee threshold; the principal stability conclusions concern the region above that threshold and do not depend on this low-density behavior.

Keywords: Filippov system; fear effect; strong Allee effect; two-threshold control; sliding mode; boundary equilibrium

1. Introduction

Threshold-based pest management makes control discontinuous. A pesticide is applied after pest density exceeds an economic level, while enemy release follows a separate rule on enemy abundance. The resulting vector field jumps across switching surfaces, so crossing solutions, sliding segments, and pseudo-equilibria must be interpreted through nonsmooth dynamics. Filippov [1] introduced the convex definition that is now standard for discontinuous right-hand sides. Kuznetsov et al. [2] classified one-parameter bifurcations in planar Filippov systems, including events at switching manifolds. Di Bernardo et al. [3] reviewed bifurcations in nonsmooth dynamical systems across impact, friction, and switching models. Andrade et al. [4] constructed bifurcation diagrams for global connections in Filippov systems. Simpson [5] analyzed the stability of boundary equilibria in three-dimensional Filippov systems. These contributions supply the nonsmooth analytical framework used below.

Threshold switching has been applied to both pest and epidemic management. Tang et al. [6] analyzed sliding bifurcations of Filippov two-stage pest-control models with economic thresholds. Zhang and Xiao [7] studied global dynamics of a Filippov epidemic system with imperfect vaccination. Wang et al. [8] classified planar Filippov systems with a delayed threshold and applied the classification to infectious disease transmission. The delayed threshold changes the switching law rather than merely shifting a constant boundary, which is one reason the no-delay setting is treated separately here.

Earlier Filippov pest models also provide the two-threshold architecture used in this paper. Tang et al. [9] formulated integrated pest-management models and examined their dynamical behavior. Zhao et al. [10] studied nonsmooth plant-disease models with economic thresholds. Kang et al. [11] analyzed a threshold-control model with group defense of pests and constant-rate release of natural enemies. Li et al. [12] investigated global dynamics of a Filippov predator–prey model with two thresholds for integrated pest management. Their switching rules motivate the three active fields considered here, but they do not include a continuous fear parameter.

Fear enters through a different route. Zanette et al. [13] showed experimentally that perceived predation risk can reduce the number of offspring produced per year. Wang et al. [14] incorporated this idea into a predator–prey model through a fear-dependent reproduction term. Hu et al. [15] studied dynamic behaviors and bifurcations of a three-dimensional Filippov ecosystem with a fear effect. Panday et al. [16] analyzed stability and bifurcation in a three-species food chain with fear. Together with these ecological mechanisms, pesticide use can alter the interaction between pests and their natural enemies: Janssen and van Rijn [17] reviewed evidence that pesticides do not necessarily reduce arthropod pest densities when natural enemies are present.

The growth term in (2.1) contains a strong Allee zero at m_0 and the additional low-density factor $x/(x + n_0)$. Wang et al. [18] used a double Allee effect in a predator–prey model for Turing-pattern analysis. Kong and Yang [19] analyzed a Filippov *Lymantria dispar*–Great tit model with double Allee effects and two-threshold control. The ecological role of Allee thresholds in invasion management was discussed by Liebhold and Tobin [20], while Tobin et al. [21] examined how Allee effects can be exploited for managing biological invasions. The terminology "double Allee effect" is not uniform. Rocha et al. [22] applied it to a discrete γ-Ricker predator–prey model with transcritical and Neimark–Sacker bifurcations. Boukal and Berec [23] reviewed single-species Allee models through extinction boundaries, sex ratios, and mate encounters. Rocha et al. [24] compared strong and weak Allee effects and chaotic dynamics in Richards-type growth. In the present paper, the phrase refers only to the two

low-density factors in (2.1); it does not imply the discrete structure or the weak-Allee mechanism from those studies.

Fear enters as $1/(1 + ky)$, so it multiplies the signed growth term rather than births alone. Below m_0, the same factor reduces the magnitude of negative growth, a modeling consequence recorded in Remark 2.1. The analysis below uses $x > m_0$, where $g > 0$. Delayed thresholds are left out because a delay would enlarge the state space. Arafa et al. [25] studied a Filippov pest-control model with a time delay. Wang and Yang [26] analyzed a non-smooth Filippov pest–natural-enemy system with a time delay. Liu and Yang [27] studied dynamics and bifurcations of a delay non-smooth Filippov Leslie–Gower prey–predator model.

Several nonsmooth ecological models are especially close to the present setting. Zhang and Tang [28] established the existence of multiple sliding segments and analyzed their bifurcations in a Filippov prey–predator model. Li [29] performed a bifurcation analysis of a Filippov predator–prey model with two thresholds. Hamdallah and Arafa [30] analyzed the stability of a Filippov prey–predator model with a fear effect and prey refuge. Sun and Xiang [31] studied a Filippov pest–natural-enemy model incorporating fear and prey refuge. Huang et al. [32] examined non-smooth dynamics of a Filippov predator–prey model with antipredator behavior. These studies establish that fear and refuge can move equilibria relative to switching boundaries, but they do not track the full equilibrium-and-sliding structure along a continuous fear parameter.

Reaction–diffusion Filippov models provide a related spatial setting. Jiao et al. [33] studied a reaction–diffusion Filippov Leslie–Gower predator–prey model with time delay and discontinuous harvesting. Lv and Li [34] analyzed a delayed reaction–diffusion Filippov system with threshold control for plateau pika–vegetation dynamics. Zhang and Yang [35] analyzed threshold control in a reaction–diffusion Filippov food chain. Those papers add diffusion, whereas the present model is spatially homogeneous; isolating the fear-induced equilibrium and sliding changes first provides a natural precursor to spatial extensions.

Related nonsmooth methods have also been developed for oscillators and maps. Miao et al. [36] studied the existence and destruction of invariant tori in a quasi-periodically forced discontinuous oscillator. Duan et al. [37] developed symbolic dynamics for a class of piecewise smooth maps. Duan et al. [38] analyzed strange nonchaotic attractors in quasiperiodically forced piecewise smooth systems. These settings are map-based or externally forced and do not imply the same behavior in the autonomous planar system studied here.

Earlier work therefore supplies the switching architecture, the Allee mechanism, and several biological ingredients. The missing piece is a continuous fear parameter carried through both the smooth equilibria and the sliding segments. We track that parameter in G_1, G_2, G_3 and on Σ_{23}. In G_1 and G_3, the enemy nullcline fixes $x^* = d/a$, and the trace becomes $\psi(d/a)/[(d/a)(1 + ky^*)]$. Its numerator is independent of k. On a hyperbolic branch, fear may cross a switching line but cannot change smooth local stability or create a Hopf bifurcation (Corollary 3.1). In G_2, equilibria satisfy $L(x; k) = 1$; the sign of L' determines the determinant sign. At $k = 0.05$, a Sturm sequence certifies two roots in $(m_0, d/a)$ (Appendix A.1). Continuation follows the branches to $k_* \approx 5.4275$; the theorem fixes this endpoint, not the number of tangencies. On Σ_{23}, the pseudo-equilibrium reaches the reduced-dose equilibrium at $k_c \approx 0.0676$, where E_3^* changes from regular to virtual. To our knowledge, this combination of a continuous fear parameter with the full two-threshold equilibrium and sliding structure has not been published elsewhere.

Removing fear clarifies the comparison. At $k = 0$, the vertical nullcline $x^* = d/a$ is unchanged; as k increases, y_i^* falls, E_3^* may cross $y = y_T$, and the F_2 equilibria disappear once $L < 1$. Each effect reduces to a scalar crossing of L. Equation (3.10) isolates the k-independent numerator, and Appendix A.1 supplies the exact baseline count. Section 2 sets the switching rule and well-posedness. Sections 3–5 treat smooth equilibria, sliding dynamics, and threshold transitions. Section 5.4 reports the numerical protocol, while Section 6 discusses the scope and limitations.

2. Model formulation

2.1. Growth, fear, and threshold control

Let $x(t)$ and $y(t)$ denote pest and natural-enemy densities. The growth term is

$$g(x) = \frac{rx}{x + n_0}\left(1 - \frac{x}{K}\right)(x - m_0), \tag{2.1}$$

where $r > 0$, $K > 0$, $0 < m_0 < K$, and $n_0 > 0$. The factor $x - m_0$ creates a strong Allee threshold at m_0, $1 - x/K$ imposes a carrying-capacity limit at K, and $x/(x + n_0)$ adds a further low-density limitation. Following the double-Allee formulations of Wang et al. [18] and Kong and Yang [19], we call g a double-Allee-type growth function. It has only one positive zero, at m_0; the word "double" refers to the two low-density mechanisms in (2.1), not to a second equilibrium threshold.

The phrase "double Allee effect" is used in several ways. For example, Rocha et al. [22] applied it to a discrete γ-Ricker predator–prey model with transcritical and Neimark–Sacker bifurcations. Here it refers only to the two low-density factors in (2.1) and does not imply that discrete structure. With $m_0 > 0$, per-capita growth is negative below m_0, so the Allee effect is strong. If $m_0 < 0$, the positive extinction threshold disappears. A weak Allee effect then requires $\varphi(x) = g(x)/x$ to increase at low density. Since $\varphi'(0) = r[Kn_0 + m_0(K + n_0)]/(Kn_0^2)$, the extra condition $Kn_0 + m_0(K + n_0) > 0$ is necessary; $m_0 < 0$ alone is not enough. We do not treat the weak case. Classical one-parameter forms that connect strong and weak effects, such as $(x - E)/(K + C)$ with $|E| < K$, were reviewed by Boukal and Berec [23] and Rocha et al. [24].

So $g(x) > 0$ for $m_0 < x < K$, whereas $g(x) < 0$ for $0 < x < m_0$ and for $x > K$. Non-consumptive fear is represented by

$$f(y) = \frac{1}{1 + ky}, \qquad k \geq 0. \tag{2.2}$$

This multiplicative form follows the classical predator–prey fear model [14]. It satisfies $f(0) = 1$ and $f'(y) = -k/(1 + ky)^2$, so $f'(y) \leq 0$, with strict inequality for $k > 0$, and $f(y) \to 0$ as $y \to \infty$ when $k > 0$.

Remark 2.1 (Interpretation of the fear term). The factor $1/(1 + ky)$ multiplies all of $g(x)$. For $x > m_0$, it lowers positive growth as y rises. For $x < m_0$, it weakens the negative term. This slowdown follows from applying fear to signed growth; it is not a separate biological assumption. A model that applies fear only to births would have a different closure. We restrict the stability and threshold claims to $x > m_0$, and draw no conclusion about fear below the Allee threshold.

Let $x_T \in (m_0, K)$ and $y_T > 0$ denote the pest and natural-enemy thresholds. The control rule is

$$(u, v) = \begin{cases} (0, 0), & x < x_T, \\ (\eta_1, \theta_1), & x > x_T,\ y < y_T, \\ (\eta_2, 0), & x > x_T,\ y > y_T, \end{cases} \tag{2.3}$$

with $\eta_1 > \eta_2 > 0$ and $\theta_1 > 0$. Figure 1 shows the three control regions and the fear response. The corresponding model is

$$\begin{aligned} \dot{x} &= \frac{g(x)}{1+ky} - bxy - ux, \\ \dot{y} &= axy - dy + v, \end{aligned} \tag{2.4}$$

where $b, a, d > 0$. The coefficient a is a composite numerical response: If e denotes conversion efficiency and b the attack rate, then $a = eb$.

Define the open regions

$$\begin{aligned} G_1 &= \{(x,y) : 0 < x < x_T < K,\ y > 0\}, \\ G_2 &= \{(x,y) : x_T < x < K,\ 0 < y < y_T\}, \\ G_3 &= \{(x,y) : x_T < x < K,\ y > y_T\}, \end{aligned} \tag{2.5}$$

and the switching manifolds

$$\begin{aligned} \Sigma_{12} &= \{x = x_T,\ 0 < y < y_T\}, \\ \Sigma_{13} &= \{x = x_T,\ y > y_T\}, \\ \Sigma_{23} &= \{x_T < x < K,\ y = y_T\}. \end{aligned} \tag{2.6}$$

Equations (2.6) are read inside the invariant rectangle $0 \le x \le K$, $y \ge 0$ from Proposition 2.1. This is why $x < K$ appears explicitly. Motion across a switching line is defined through the Filippov convex hull [1]. At $C = (x_T, y_T)$, three fields meet and continuation need not be unique. In the simulations, F_1 is tested first only when a trajectory reaches C exactly. The equilibrium and sliding results do not use this convention.

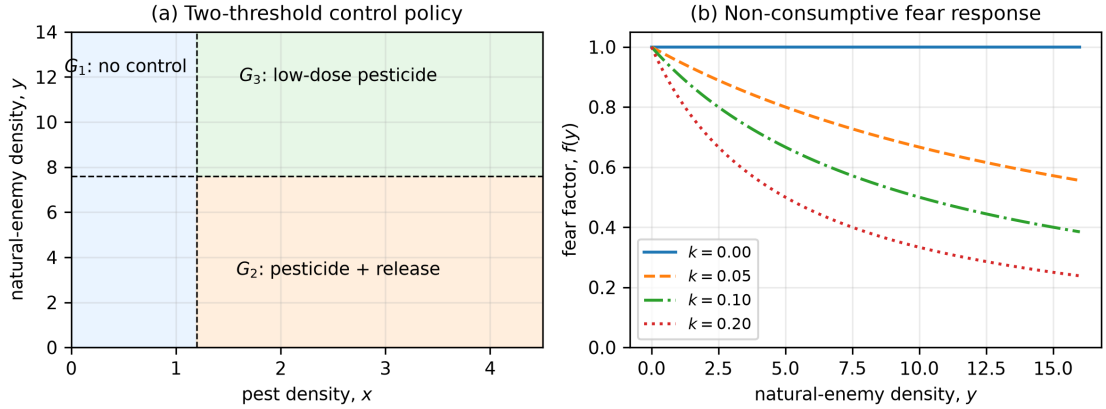


Figure 1. (a) Two-threshold control regions and the three active vector fields. (b) The decreasing fear factor $f(y) = 1/(1 + ky)$ for several values of the fear intensity.

2.2. Parameter scenario

Table 1 lists the dimensionless values used in the baseline calculations. They are illustrative, not fitted to a particular pest system.

We assume $m_0 < x_T < K$ and $d/a \in (m_0, K)$. All variables and parameters are normalized; no field calibration is implied. Numerical integration is restricted to $0 \le x \le K$ and $y \le 30$, and trajectories that leave this rectangle are reported rather than truncated.

Table 1. Dimensionless parameter values for the baseline calculations.

Symbol	Meaning	Baseline
r	pest intrinsic growth rate	2.00
K	carrying capacity	4.50
n_0	low-density saturation parameter	0.30
m_0	Allee threshold	0.10
b	attack coefficient	0.08
a	composite numerical response	0.40
d	natural-enemy mortality	0.50
η_1	pesticide rate in G_2	0.20
η_2	pesticide rate in G_3	0.10
θ_1	release rate	0.15
k	fear intensity	0.05
x_T	pest threshold	1.20
y_T	enemy threshold	7.60

The analytical results use $r, K, n_0, b, a, d, \theta_1 > 0$, $\eta_1 > \eta_2 > 0$, $0 < m_0 < K$, $m_0 < x_T < K$, $y_T > 0$, and $d/a \in (m_0, K)$. Two quantities are varied: the fear intensity $k \in [0, \infty)$, which is the bifurcation parameter in Sections 3–5, and the enemy threshold y_T, scanned over $5 \le y_T \le 10$ in Figure 5. Table 4 also reports one-percent changes in a, d, and x_T. These positivity and ordering inequalities define the free parameter ranges; only Table 1 fixes the numerical baseline.

2.3. Positive invariance and dissipativity

Proposition 2.1 (Positive invariance and an ultimate bound)**.** *Assume $0 \le x(0) \le K$ and $y(0) \ge 0$. Then every Filippov solution of (2.3) and (2.4) satisfies, for every $t \ge 0$, $0 \le x(t) \le K$ and $y(t) \ge 0$ for all $t \ge 0$. Moreover,*

$$\limsup_{t\to\infty} \left[x(t) + \frac{b}{a} y(t) \right] \le K + \frac{g_M + (b/a)\theta_1}{d}, \tag{2.7}$$

where $g_M = \max_{0\le x\le K} g(x)$. Every solution with initial data in the invariant rectangle is ultimately bounded.

Proof. At $x = 0$, $\dot{x} = 0$. At $x = K$, $g(K) = 0$ and

$$\dot{x} = -bKy - uK \le 0.$$

For $x > K$, $g(x) < 0$, so the right-hand side of $\dot{x}$ remains negative. The interval $[0, K]$ is positively invariant for each smooth field and for every convex combination. At $y = 0$, $\dot{y} = v \ge 0$, with $v \le \theta_1$ on every convex combination; so $y(t) \ge 0$.

To obtain the dissipativity bound, define $z = x + (b/a)y$. Using (2.4),

$$\dot{z} = \frac{g(x)}{1 + ky} - ux - \frac{bd}{a} y + \frac{b}{a} v \le g_M + \frac{b\theta_1}{a} - d(z - x).$$

Since $x \le K$ and $z \ge x$, for $z > K$,

$$\dot{z} \le g_M + \frac{b\theta_1}{a} - d(z - K).$$

By the comparison principle,

$$\limsup_{t\to\infty} z(t) \le K + \frac{g_M + (b/a)\theta_1}{d},$$

which is (2.7). Both coordinates are ultimately bounded. □

Each smooth field is locally Lipschitz. After Filippov regularization, the set-valued field is upper semicontinuous, locally bounded, and convex-valued. An absolutely continuous solution starts from every point of the invariant rectangle. Proposition 2.1 rules out finite-time escape, so solutions extend to all $t \ge 0$. We do not need uniqueness at tangencies or at C.

Remark 2.2 (Corner convention). At $C = (x_T, y_T)$, three limiting fields meet, so the standard Filippov set may be multivalued. In the numerical code, F_1 is tested first only when a trajectory hits C exactly. This restart rule does not enter the equilibrium or sliding analysis, and none of the representative runs or the 40×40 diagnostic grid reached C.

3. Smooth subsystems

Let $F_i = (F_i^x, F_i^y)^\mathsf{T}$, $i = 1, 2, 3$, be the fields obtained from (2.4) with $(u_i, v_i) = (0, 0), (\eta_1, \theta_1), (\eta_2, 0)$ in that order. An equilibrium of F_i is called *positive* when $x > 0$ and $y > 0$, *regular* when it lies in G_i, *virtual* when it lies outside the closure of G_i, and a *switching-boundary equilibrium* when it lies on a switching manifold. Equilibria on $x = 0$ or $y = 0$ are listed separately as *state boundary equilibria*. The next three subsections describe the equilibria of each field and their local stability.

Hyperbolicity convention All local stability statements below refer to hyperbolic equilibria. If the relevant nondegeneracy condition fails, the linearization is not conclusive; such points require a center-manifold or higher-order analysis and are not classified from the signs of the trace and determinant alone.

3.1. Axis and predator-free equilibria

On $y = 0$, the enemy equation for F_1 and F_3 is $\dot{y} = (ax - d)y$. Nonzero predator-free equilibria of these fields satisfy

$$g(x) = u_i x, \qquad u_1 = 0, \quad u_3 = \eta_2, \tag{3.1}$$

where $x = 0$ is an additional root introduced by the factor x in the pest equation. The field F_2 has no equilibrium on $y = 0$ because $F_2^y(x, 0) = \theta_1 > 0$. Its only equilibrium with $x = 0$ is

$$E_2^0 = \left(0, \frac{\theta_1}{d}\right), \tag{3.2}$$

which is virtual for G_2 because $x_T > 0$. The Jacobian at this point is lower triangular with diagonal entries

$$\frac{g'(0)}{1 + k\theta_1/d} - \frac{b\theta_1}{d} - \eta_1 < 0, \qquad -d < 0,$$

so E_2^0 is a stable node of the F_2 field.

For $x > 0$, define

$$\varphi(x) := \frac{g(x)}{x} = \frac{r}{x + n_0}\left(1 - \frac{x}{K}\right)(x - m_0). \tag{3.3}$$

The nonzero predator-free equilibria of F_3 are the roots of $\varphi(x) = \eta_2$.

Proposition 3.1 (Axis equilibria)**.** *Assume $m_0 < x^* = d/a < K$. For F_1, $E_0 = (0,0)$ is a stable node, whereas $E_m = (m_0, 0)$ and $E_K = (K, 0)$ are saddles. For F_3, E_0 remains a stable node, but $(m_0, 0)$ and $(K, 0)$ are not equilibria. The positive predator-free equilibria of F_3 are the roots of $\varphi(x) = \eta_2$, classified in Lemma 3.1.*

Proof. At $(0,0)$, the Jacobian of F_i is diagonal with entries $-rm_0/n_0 - u_i < 0$ and $-d < 0$; hence E_0 is a stable node for $i = 1, 3$. For F_1, the Jacobian at $(x, 0)$, $x > 0$, is

$$\begin{pmatrix} g'(x) & -bx \\ 0 & ax - d \end{pmatrix}.$$

At $x = m_0$, the eigenvalues are $g'(m_0) > 0$ and $am_0 - d < 0$; at $x = K$, they are $g'(K) < 0$ and $aK - d > 0$. Both points are saddles. For F_3, $F_3^x(m_0, 0) = -\eta_2 m_0 \neq 0$ and $F_3^x(K, 0) = -\eta_2 K \neq 0$, so $(m_0, 0)$ and $(K, 0)$ are not equilibria. The remaining predator-free equilibria of F_3 are covered by Lemma 3.1. □

Lemma 3.1 (Predator-free equilibria of the extended F_3)**.** *The function φ has a unique critical point*

$$x_M = \sqrt{(n_0 + K)(n_0 + m_0)} - n_0 \in (m_0, K), \tag{3.4}$$

which is a strict maximum, with $\varphi_M := \varphi(x_M) > 0$. The number of roots falls into three cases:

(i) if $0 < \eta_2 < \varphi_M$, the equation $\varphi(x) = \eta_2$ has exactly two roots $x_- \in (m_0, x_M)$ and $x_+ \in (x_M, K)$;

(ii) if $\eta_2 = \varphi_M$, it has the double root x_M;

(iii) if $\eta_2 > \varphi_M$, it has no positive root.

At a root $x_r \in \{x_-, x_+\}$, the Jacobian of F_3 at $(x_r, 0)$ has eigenvalues

$$\lambda_1 = x_r \varphi'(x_r), \qquad \lambda_2 = a(x_r - x^*), \qquad x^* = \frac{d}{a}. \tag{3.5}$$

Since $\varphi'(x_-) > 0$ and $\varphi'(x_+) < 0$, the first eigenvalue is positive at x_- and negative at x_+. The second eigenvalue $a(x_r - x^*)$ depends on the relative position of x_r and x^*. So $(x_-, 0)$ is a saddle if $x_- < x^*$, an unstable node if $x_- > x^*$, and nonhyperbolic if $x_- = x^*$; $(x_+, 0)$ is a stable node if $x_+ < x^*$, a saddle if $x_+ > x^*$, and nonhyperbolic if $x_+ = x^*$. At $\eta_2 = \varphi_M$, x_M is a double root and is nonhyperbolic.

Proof. At $x > 0$,

$$\varphi'(x) = -\frac{r}{K} \frac{x^2 + 2n_0 x - Km_0 - n_0(K + m_0)}{(x + n_0)^2}.$$

The numerator is a concave quadratic with one positive zero, x_M. Since $\varphi > 0$ on (m_0, K) and vanishes at both endpoints, this zero is a strict maximum and $\varphi_M > 0$. The three cases follow. At $(x_r, 0)$,

$$J_3(x_r, 0) = \begin{pmatrix} g'(x_r) - \eta_2 & -kg(x_r) - bx_r \\ 0 & ax_r - d \end{pmatrix},$$

and $g'(x_r) - \eta_2 = x_r \varphi'(x_r)$ because $\varphi(x_r) = \eta_2$. Since $g(x_r) = x_r \eta_2$, the upper-right entry is also $-(b + k\eta_2)x_r$. The matrix remains triangular, so (3.5) is unchanged. The sign of φ' is positive on (m_0, x_M) and negative on (x_M, K). So $\lambda_1 > 0$ at x_- and $\lambda_1 < 0$ at x_+. The sign of $\lambda_2 = a(x_r - x^*)$ is determined separately by the ordering of x_r and x^*; no ordering between x_- and x^* follows from $x^* \in (m_0, K)$. The double-root case has $\lambda_1 = 0$. □

Remark 3.1 (Nonhyperbolic predator-free cases). If $x_\pm = x^*$ or $\eta_2 = \varphi_M$, the corresponding predator-free equilibrium is nonhyperbolic. Linearization does not determine its stability, and it is not classified further here.

Remark 3.2. The roots $x_\pm$ are predator-free equilibria of the algebraic subsystem. They are virtual in the original piecewise field because $y = 0 < y_T$. This distinction is used in the regular/virtual classification of Section 5.

3.2. Positive equilibria of the extended fields F_1 and F_3

Let

$$x^* := \frac{d}{a}, \qquad A_0 := \varphi(x^*) = \frac{g(x^*)}{x^*}. \tag{3.6}$$

Assume $m_0 < x^* < K$, so that $A_0 > 0$. The hyperbolicity condition for E_1^* and E_3^* is $\psi(x^*) \neq 0$. If $\psi(x^*) = 0$, the equilibrium is nonhyperbolic and the stability statements below do not apply. The following proposition collects the model-specific formulas used repeatedly in later sections.

Proposition 3.2 (Positive equilibria of the extended fields F_1 and F_3)**.** *The following statements hold.*

(i) The extended field F_1 has a positive equilibrium $E_1^* = (x^*, y_1^*(k))$ if and only if $m_0 < x^* < K$, where

$$y_1^*(k) = \begin{cases} \dfrac{-b + \sqrt{b^2 + 4bkA_0}}{2bk}, & k > 0, \\ \dfrac{A_0}{b}, & k = 0. \end{cases} \tag{3.7}$$

(ii) The extended field F_3 has a positive equilibrium $E_3^* = (x^*, y_3^*(k))$ if and only if $m_0 < x^* < K$ and $A_0 > \eta_2$, where, with $\Delta_3 := (b + k\eta_2)^2 + 4bk(A_0 - \eta_2)$,

$$y_3^*(k) = \begin{cases} \dfrac{-(b + k\eta_2) + \sqrt{\Delta_3}}{2bk}, & k > 0, \\ \dfrac{A_0 - \eta_2}{b}, & k = 0. \end{cases} \tag{3.8}$$

(iii) For $i = 1, 3$, the Jacobian at E_i^* satisfies

$$\det J_i = \left(bx^* + \frac{kg(x^*)}{(1 + ky_i^*)^2} \right) ay_i^* > 0, \tag{3.9}$$

and the trace factorizes as

$$T_i(k) := \operatorname{tr} J_i = \frac{\psi(x^*)}{x^*(1 + ky_i^*)}, \qquad \psi(x) := xg'(x) - g(x). \tag{3.10}$$

The sign of $\psi(x^*)$ gives the local stability type: negative for asymptotic stability, positive for instability, and zero for a nonhyperbolic point. This sign does not depend on k.

(iv) Both $y_1^*(k)$ and $y_3^*(k)$ are strictly decreasing in k. The fear loads

$$L_i^*(k) := \frac{ky_i^*(k)}{1 + ky_i^*(k)} \tag{3.11}$$

satisfy

$$L_1^*(k) = 1 - \frac{by_1^*(k)}{A_0}, \qquad L_3^*(k) = 1 - \frac{by_3^*(k) + \eta_2}{A_0}, \tag{3.12}$$

and are strictly increasing in k.

Proof. At a positive equilibrium of F_i ($i = 1, 3$), setting $\dot{y} = 0$ gives $x = x^*$. Substitution into $\dot{x} = 0$ gives

$$\frac{A_0}{1 + ky} = by + u_i,$$

where $u_1 = 0$ and $u_3 = \eta_2$. This gives a quadratic equation in y; selecting its positive root gives (3.7) and (3.8). The determinant formula follows directly from the Jacobian

$$J_i = \begin{pmatrix} \dfrac{g'(x^*)}{1 + ky_i^*} - by_i^* - u_i & -\dfrac{kg(x^*)}{(1 + ky_i^*)^2} - bx^* \\ ay_i^* & 0 \end{pmatrix}. \tag{3.13}$$

For the trace, the equilibrium identity

$$\frac{g(x^*)}{1 + ky_i^*} = x^*(by_i^* + u_i) \tag{3.14}$$

gives $by_i^* + u_i = g(x^*)/[x^*(1 + ky_i^*)]$. Substituting this into the $(1, 1)$ entry yields

$$T_i(k) = \frac{g'(x^*)}{1 + ky_i^*} - \frac{g(x^*)}{x^*(1 + ky_i^*)} = \frac{x^*g'(x^*) - g(x^*)}{x^*(1 + ky_i^*)},$$

which is (3.10). Local stability follows from $\det J_i > 0$ and the Routh–Hurwitz criterion. Finally, differentiating the equilibrium identity with respect to k gives

$$y_i^{*\prime}(k) = -\frac{y_i^*(by_i^* + u_i)}{b(1 + 2ky_i^*) + ku_i} < 0,$$

and (3.12) follows by rearranging the identity. □

Corollary 3.1 (No fear-driven trace crossing in the extended F_1 and F_3 fields)**.** *For each relevant field $i = 1, 3$, assume that the positive equilibrium exists. If $\psi(x^*) \neq 0$, then $T_i(k) \neq 0$ for every admissible k. Changing k alone cannot produce a smooth Hopf bifurcation of E_1^* or E_3^* within the corresponding admissible interval.*

Proof. Equation (3.10) shows that the sign of $T_i(k)$ is the sign of $\psi(x^*)$, while the denominator is positive. $T_i(k)$ cannot change sign unless $\psi(x^*) = 0$. □

Remark 3.3. Corollary 3.1 treats k as the only varying parameter. Since $\psi(x_M) = 0$, a second parameter can move $x^* = d/a$ across x_M and restore the classical Hopf scenario. The factorization (3.10) then separates the criticality calculation from the fear response.

Corollary 3.2 (Explicit stability classification for the extended F_1 and F_3 fields)**.** *For each $i = 1, 3$, assume that the positive equilibrium $E_i^* = (x^*, y_i^*)$ exists. If $x^* > x_M$, then E_i^* is locally asymptotically stable; if $x^* < x_M$, then E_i^* is unstable; if $x^* = x_M$, then E_i^* is nonhyperbolic and the linearization is inconclusive.*

Proof. Since $\varphi(x) = g(x)/x$, we have $\psi(x) = xg'(x) - g(x) = x^2\varphi'(x)$. Lemma 3.1 gives $\varphi'(x) > 0$ on (m_0, x_M) and $\varphi'(x) < 0$ on (x_M, K). By (3.10), the sign of $T_i(k)$ equals the sign of $\psi(x^*)$, and $\det J_i > 0$ whenever the equilibrium exists. This proves the stated stability classification. At $x^* = x_M$, $\psi(x^*) = 0$, so the equilibrium is nonhyperbolic and the linearization is inconclusive. □

Remark 3.4 (Biological significance of Corollaries 3.1 and 3.2). The two corollaries can be read ecologically. In G_1 and G_3, raising k lowers $y_i^*(k)$, but $x^* = d/a$ and the trace sign stay fixed. Fear cannot create a smooth Hopf oscillation in either region. It can move E_3^* across $y = y_T$, and this changes whether the equilibrium is regular or virtual. The stability boundary is $x^* = x_M$. If $x^* > x_M$, per-capita growth falls with density and coexistence is stabilized; if $x^* < x_M$, the positive slope on the Allee side acts in the opposite direction. A change in d/a can therefore affect stability even when fear alone cannot.

For the baseline parameters,

$$\psi(x^*) = x^*g'(x^*) - g(x^*) \approx -0.1395 < 0, \tag{3.15}$$

and $x_M \approx 1.0856 < x^* = 1.25$, so Corollary 3.2 gives the same conclusion. Within the smooth extensions, E_1^* and E_3^* are locally asymptotically stable whenever they exist. In the piecewise model this holds only while the point remains regular. At $k = 0.05$, $E_1^* \approx (1.25, 9.1813)$ and $E_3^* \approx (1.25, 8.2380)$. The first is virtual in G_1, because $x^* > x_T$. The second stays regular in G_3 until k_c, where it reaches the switching boundary.

3.3. Positive equilibria and local stability in the extended field F_2

For G_2, the enemy nullcline is

$$y = \frac{\theta_1}{d - ax}, \qquad 0 < x < \frac{d}{a}. \tag{3.16}$$

Define

$$\begin{aligned} w(x) &:= d - ax, \qquad P(x) := g(x)w(x)^2, \\ R(x;k) &:= x\left[b\theta_1 + \eta_1 w(x)\right]\left[w(x) + k\theta_1\right], \end{aligned} \tag{3.17}$$

and

$$L(x;k) := \frac{P(x)}{R(x;k)}. \tag{3.18}$$

For $x > 0$, $L = 1$ is equivalent to $Q_2(x;k) = 0$, where

$$\begin{aligned} Q_2(x;k) := {} & r(K - x)(x - m_0)w(x)^2 \\ & - K(x + n_0)[b\theta_1 + \eta_1 w(x)][w(x) + k\theta_1]. \end{aligned} \tag{3.19}$$

Indeed, Q_2 is obtained from $P - R$ by multiplying by the positive factor $K(x + n_0)/x$. Thus F_2 has a positive equilibrium exactly when $L(x;k) = 1$, $x \in (m_0, d/a)$, with $y = \theta_1/w(x)$.

In the F_2 stability statements below, a transversal positive equilibrium is considered hyperbolic when $L'(x;k) \neq 0$ and, if $\det J_2 > 0$, $T_2(x;k) \neq 0$. If either condition fails, the Jacobian is nonhyperbolic and no stability conclusion is drawn.

Theorem 3.1 (Positive equilibria and terminal loss-of-equilibria threshold in F_2)**.**

(i) With $L(d/a;0) := 0$, we have $L(m_0;k) = 0$ for every $k \geq 0$, $L(d/a;k) = 0$ for $k > 0$, and $L(x;k) > 0$ on $(m_0, d/a)$. Every positive equilibrium is therefore a transverse or tangential crossing of $L = 1$.

(ii) Let $\mathcal{M}(k) = \max_{x\in[m_0,d/a]} L(x;k)$. If $\mathcal{M}(k) < 1$, F_2 has no positive equilibrium. If $\mathcal{M}(k) = 1$, some $x_\dagger \in (m_0, d/a)$ satisfies $L(x_\dagger;k) = 1$ and $L'(x_\dagger;k) = 0$. If $\mathcal{M}(k) > 1$, the set $\{x : L(x;k) > 1\}$ has at least one component. When 1 is a regular value, each component contributes exactly two roots and there are no other roots. Counting the roots requires fixed coefficients; Appendix A.1 treats $Q_2(x; 0.05)$. A fold also needs $L''(x_\dagger;k) \neq 0$ and transversality in the varied parameter.

(iii) At a positive equilibrium x, the trace of the Jacobian of F_2 is

$$T_2(x;k) = \frac{g'(x)w(x)}{w(x)+k\theta_1} - \frac{b\theta_1}{w(x)} - \eta_1 - w(x), \tag{3.20}$$

and the determinant is

$$\det J_2 = -x\left[b\theta_1 + \eta_1 w(x)\right] L'(x;k), \tag{3.21}$$

where the derivative is with respect to x. At a positive equilibrium, $L' > 0$ gives a saddle. If $L' < 0$, the determinant is positive: $T_2 < 0$ gives local asymptotic stability and $T_2 > 0$ gives instability. At $T_2 = 0$, the linearization is nonhyperbolic. A Hopf bifurcation then needs separate transversality and higher-order conditions; (3.20) and (3.21) alone do not settle stability.

(iv) Geometrically, the last positive component disappears when $\max_x L(x;k)$ falls through one. If $\max_x L(x;0) > 1$, this happens at a unique terminal threshold $k_* > 0$, with $\max_x L(x;k_*) = 1$. Only the threshold is unique; the maximizing tangency need not be. For $0 \leq k < k_*$, there are at least two positive equilibria, and for $k > k_*$ there are none. At $k = k_*$, at least one point has $L = 1$, $L' = 0$, and $\det J_2 = 0$. We do not prove uniqueness of this tangency. A nondegenerate fold also requires $L'' \neq 0$ and $L_k \neq 0$.

Proof. The endpoint values follow from $g(m_0) = 0$, $w(d/a) = 0$ and the positivity of the remaining factors on $(m_0, d/a)$. Every equilibrium obeys $L = 1$; continuity and the endpoint values then determine the possible number of crossings. (iii) Define

$$N(x) := F_2^x\left(x, \frac{\theta_1}{w(x)}\right).$$

A direct calculation gives

$$N(x) = \frac{P(x) - R(x;k)}{w(x)\left[w(x)+k\theta_1\right]}.$$

At a root $L = 1$, $P = R$, and therefore

$$N'(x) = \frac{R(x;k)}{w(x)\left[w(x)+k\theta_1\right]} L'(x;k).$$

Since the Jacobian is

$$J_2 = \begin{pmatrix} H_x & H_y \\ ay & -w \end{pmatrix}, \qquad N'(x) = H_x + \frac{ay}{w} H_y,$$

where $H = F_2^x$, the identity $\det J_2 = -wN'(x)$ follows. Substituting the expression for N' gives (3.21). The trace formula follows by evaluating the Jacobian at the root. The sign statements and the Routh–Hurwitz criterion give the local stability conclusion. (iv) For $0 \le k_1 < k_2$, let x_m be a maximizer of $L(\cdot; k_2)$. Since L vanishes at both endpoints and is positive in the interior, $x_m \in (m_0, d/a)$. Pointwise monotonicity in k gives

$$\mathcal{M}(k_1) \ge L(x_m; k_1) > L(x_m; k_2) = \mathcal{M}(k_2).$$

Thus $\mathcal{M}$ decreases strictly with k. The extension makes L continuous on a compact interval, so $\mathcal{M}$ is continuous. For $k > 0$, $L(x; k) \le C/k$ uniformly in x, and hence $\mathcal{M}(k) \to 0$ as $k \to \infty$. If $\mathcal{M}(0) > 1$, there is a unique k_* such that $\mathcal{M}(k_*) = 1$. At least one interior maximizer x_f satisfies $L(x_f; k_*) = 1$ and $L_x(x_f; k_*) = 0$, so $\det J_2 = 0$. A fold requires further nondegeneracy conditions. Away from the tangency, part (ii) supplies the root count. □

Remark 3.5. In G_2, identity (3.21) plays the role that (3.10) plays in G_1 and G_3: the slope of L fixes the determinant sign. The equation $L' = 0$ is polynomial of degree at most six, so Sturm isolation can count its roots once the coefficients are fixed. That count describes branches; it does not by itself prove the uniqueness of a fold.

For the baseline parameters, $\max_x L(x; 0.05) = 3.850939$, so the extended F_2 field has at least two positive equilibria. A finite search in $x \in (m_0, d/a)$ locates two interior roots at $k = 0.05$:

$$(0.15441, 0.34228), \qquad (1.19889, 7.33681). \tag{3.22}$$

For fixed $k > 0$, Q_2 in (3.19) is a quartic. At $k = 0.05$, the Sturm count in Appendix A.1 shows that $Q_2(\cdot; 0.05)$ has exactly two distinct zeros in $(m_0, d/a)$. The two roots in (3.22) are therefore certified at the baseline. The statement that the sampled branch remains single for all $k \in [0, k_*]$ is numerical.

At $k = 0.05$, both roots are virtual because their pest coordinates lie below $x_T = 1.2$. The lower root is a saddle ($L' > 0$, $T_2 \approx 0.1217$, $\det J_2 \approx -0.2434$). The upper root is a stable focus ($L' < 0$, $T_2 \approx -0.0771$, $\det J_2 \approx 0.3839$). It becomes regular in G_2 for

$$k_{23}^{\text{left}} < k < k_{12}^{\text{lower}}.$$

Numerical continuation gives $E_2^+ \approx (1.20066, 7.6000)$ at the first endpoint and $E_2^+ \approx (1.20000, 7.5000)$ at the second. Between these values, $x_T < x < 1.20066$ and $7.5000 < y < y_T$, so the root lies in the open region G_2. Throughout the interval, $L_x < 0$ and $T_2 < 0$, which makes E_2^+ locally asymptotically stable as an equilibrium of F_2. Outside the interval it is virtual for G_2. Theorem 3.1(iv) places the final loss-of-equilibria threshold at $k_* \approx 5.4275$, with $x_f \approx 0.4729$. Sampling $L_x = 0$ and tracking roots for $k \in [0, k_*]$ indicates one critical branch. Within this range, the two roots persist until the loss-of-equilibria threshold. This observation is numerical and refers to the baseline parameters.

Table 2 lists the baseline coordinates, local types, and regular or virtual statuses.

Scope of the stability conclusions. The Jacobian calculations above apply to the smooth extensions F_i. In the piecewise system, they describe only regular points inside G_i. Virtual points and points on a switching manifold are handled separately. Boundary and pseudo-equilibria are treated in Section 4. None of these local tests gives a global basin.

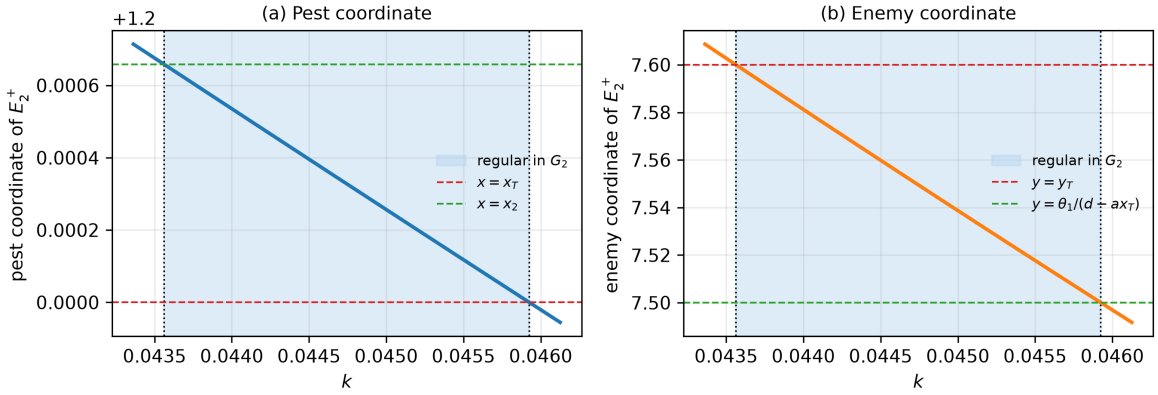


Figure 2. Regular window of the upper F_2 equilibrium for the baseline parameters. (a) The pest coordinate decreases from the horizontal switching boundary to the vertical switching boundary. (b) The enemy coordinate decreases from y_T to $\theta_1/(d - a\,x_T)$. The shaded interval marks the values of k for which the upper root lies in G_2.

Table 2. Baseline equilibria of the three smooth fields. "Regular" means that the equilibrium lies in the open region where the field is active; "Virtual" means that it is outside the closure of the active region. Points with $y = 0$ are labeled state boundary equilibria. The values are for $k = 0.05$ when the equilibrium depends on k.

Field	Equilibrium	Coordinates	Local type	State
F_1	E_0	$(0, 0)$	stable node	state boundary in closure of G_1
F_1	E_m	$(m_0, 0) = (0.1, 0)$	saddle	state boundary in closure of G_1
F_1	E_K	$(K, 0) = (4.5, 0)$	saddle	state boundary; virtual for G_1
F_1	E_1^*	$(1.25, 9.181271)$	stable focus	virtual
F_2	E_2^0	$(0, 0.3)$	stable node	state boundary; virtual for G_2
F_2	G_2-root 1	$(0.154414, 0.342283)$	saddle	virtual
F_2	G_2-root 2	$(1.198888, 7.336808)$	stable focus	virtual
F_3	E_0	$(0, 0)$	stable node	state boundary; virtual for G_3
F_3	x_-	$(0.121669, 0)$	saddle	state boundary; virtual for G_3
F_3	x_+	$(4.253331, 0)$	saddle	state boundary; virtual for G_3
F_3	E_3^*	$(1.25, 8.237974)$	stable focus	regular in G_3

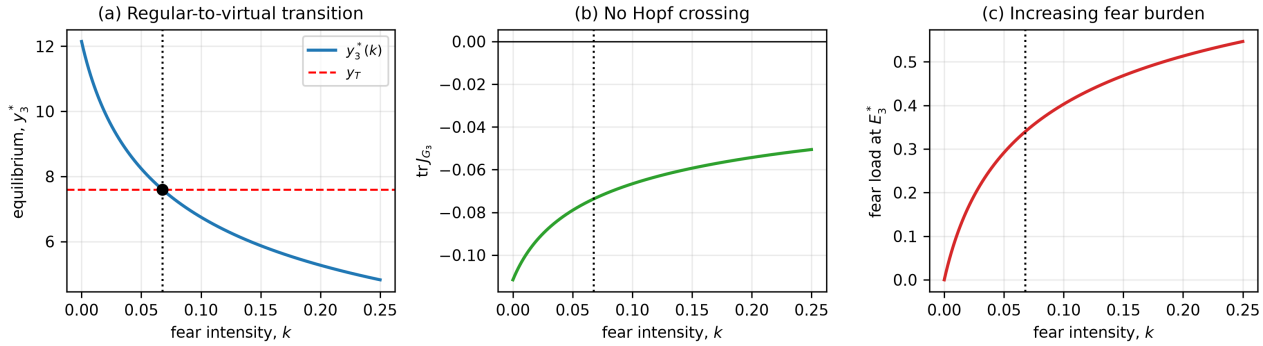


Figure 3. Fear changes the G_3 equilibrium. (a) $y_3^*(k)$ decreases and reaches y_T at $k_c \approx 0.0676$. (b) The trace remains negative over the displayed interval, consistent with (3.10). (c) The fear load $L_3^*(k)$ increases with k.

4. Sliding dynamics and pseudo-equilibria

4.1. The vertical manifolds

Throughout this section, $y_1(k), y_2(k), y_3(k)$ denote tangent roots on the switching manifolds. They are distinct from the equilibrium ordinates $y_1^*(k), y_3^*(k)$ of Section 3. Table 3 lists these and related symbols.

Table 3. Notation for the threshold, equilibrium, tangent-root, and pseudo-equilibrium coordinates.

Symbol	Meaning
y_T	fixed enemy threshold in the control rule (2.3)
$y_1^*(k), y_3^*(k)$	enemy ordinates of the positive equilibria E_1^*, E_3^* of the extended fields F_1, F_3
$y_1(k)$	tangent root of $N_1(y;k) = 0$ on Σ_{12} and Σ_{13}
$y_2(k)$	tangent root of $N_1(y;k) = \eta_1 x_T$ on Σ_{12}
$y_3(k)$	tangent root of $N_1(y;k) = \eta_2 x_T$ on Σ_{13}
$y_{p12}(k)$	enemy ordinate of the pseudo-equilibrium P_{12} on Σ_{12}
$x_{p23}(k)$	pest ordinate of the pseudo-equilibrium P_{23} on Σ_{23}

We use the standard Filippov procedure on each switching manifold. First, compute the two normal components and locate the interval where they have opposite signs. A convex combination then removes the normal component, and zeros of the remaining scalar field locate pseudo-equilibria in that interval. On Σ_{12} and Σ_{13}, pest density stays at x_T while enemy density changes. A pseudo-equilibrium there represents coexistence held at the threshold, with the control term balancing net pest growth.

On Σ_{12}, $x = x_T$ and $0 < y < y_T$. Define

$$N_1(y;k) = \frac{g(x_T)}{1+ky} - bx_T y. \tag{4.1}$$

The normal components of F_1 and F_2 are N_1 and $N_1 - \eta_1 x_T$, respectively. Since

$$\frac{\partial N_1}{\partial y} = -\frac{kg(x_T)}{(1+ky)^2} - bx_T < 0, \tag{4.2}$$

the equation $N_1 = 0$ has a unique positive root $y_1(k)$. If $g(x_T) > \eta_1 x_T$, the equation $N_1 = \eta_1 x_T$ has a unique positive root $y_2(k)$; otherwise, we set $y_2(k) = 0$. The two roots satisfy $y_2(k) < y_1(k)$. Sliding occurs on

$$I_{12}(k) = \{y : \max(0, y_2(k)) < y < \min(y_1(k), y_T)\}. \tag{4.3}$$

Here and below, $|\Sigma_{sij}|$ denotes the length of I_{ij}. The equivalent control is

$$\lambda_{12}(y; k) = \frac{N_1(y; k)}{\eta_1 x_T}, \tag{4.4}$$

and the sliding equation is

$$\dot{y} = qy + \lambda_{12}(y; k)\theta_1, \qquad q = ax_T - d. \tag{4.5}$$

A pseudo-equilibrium $P_{12} = (x_T, y_{p12})$ satisfies

$$ka_{12}y^2 + a_{12}y + c_{12} = 0, \tag{4.6}$$

where

$$a_{12} = q - \frac{\theta_1 b}{\eta_1}, \qquad c_{12} = \frac{\theta_1 g(x_T)}{\eta_1 x_T}. \tag{4.7}$$

For the baseline, $a_{12} = -0.08 < 0$, $c_{12} > 0$, and the unique positive root is

$$y_{p12}(k) = \frac{-a_{12} - \sqrt{a_{12}^2 - 4ka_{12}c_{12}}}{2ka_{12}}, \qquad k > 0. \tag{4.8}$$

At $k = 0$, the same equation gives

$$y_{p12}(0) = -\frac{c_{12}}{a_{12}}. \tag{4.9}$$

When $a_{12} < 0$, (4.6) can be written as $y_{p12} + ky_{p12}^2 = -c_{12}/a_{12} > 0$. Implicit differentiation gives

$$\frac{\mathrm{d}y_{p12}}{\mathrm{d}k} = -\frac{y_{p12}^2}{1 + 2ky_{p12}} < 0. \tag{4.10}$$

Thus the vertical pseudo-equilibrium moves downward with k whenever it is admissible. It is admissible when it lies in $I_{12}(k)$. From

$$S'_{12}(y) = q - \frac{\theta_1}{\eta_1 x_T}\left(\frac{kg(x_T)}{(1 + ky)^2} + bx_T\right), \tag{4.11}$$

it follows that $S'_{12}(y) < 0$ whenever $q \le 0$. More generally, an admissible P_{12} is locally asymptotically stable on the sliding manifold when $S'_{12}(y_{p12}) < 0$. On I_{12}, the normal components satisfy $F_1^x = N_1 > 0$ and $F_2^x = N_1 - \eta_1 x_T < 0$, so the sliding segment is transversely attracting. Together with $S'_{12} < 0$, this makes the admissible pseudo-equilibrium locally asymptotically stable for the Filippov system. At $k = 0.05$,

$$y_1 \approx 9.2065, \quad y_2 \approx 7.3363, \quad y_{p12} \approx 7.3686. \tag{4.12}$$

On Σ_{13}, $x = x_T$ and $y > y_T$. The roots are $y_1(k)$ and, if $g(x_T) > \eta_2 x_T$, the unique positive solution $y_3(k)$ of

$$N_1(y; k) = \eta_2 x_T; \tag{4.13}$$

if $g(x_T) \le \eta_2 x_T$, we set $y_3(k) = 0$. The sliding interval is

$$I_{13}(k) = \{y : \max(y_3(k), y_T) < y < y_1(k)\}, \tag{4.14}$$

and the sliding equation is

$$\dot{y} = qy. \tag{4.15}$$

For the baseline, $q = -0.02 < 0$. Thus I_{13} contains no positive pseudo-equilibrium; a trajectory on this segment either leaves through an endpoint or reaches the corner.

4.2. The horizontal switching manifold

On Σ_{23}, the normal components come from the y-equations of F_2 and F_3. A convex weight μ on F_3 cancels the normal motion, and the scalar field S_{23} describes pest density along the enemy threshold. In ecological terms, release and reduced spraying hold y at y_T while the pest density changes. We write $Y = y_T$. On Σ_{23}, the normal components of F_2 and F_3 are

$$M_2(x) = aY(x - x_2), \qquad M_3(x) = aY\left(x - \frac{d}{a}\right), \tag{4.16}$$

where

$$x_2 = \frac{d}{a} - \frac{\theta_1}{aY}. \tag{4.17}$$

Thus, with

$$x_L \coloneqq \max\{x_T, x_2\}, \tag{4.18}$$

the sliding set is

$$I_{23} = \left(x_L, \frac{d}{a}\right) \cap (x_T, K). \tag{4.19}$$

Let $\mu \in [0, 1]$ denote the coefficient of F_3 in the convex combination

$$F_\mu = (1 - \mu)F_2 + \mu F_3.$$

The normal component vanishes when

$$\mu = \frac{M_2}{M_2 - M_3} = \frac{M_2}{\theta_1}. \tag{4.20}$$

On I_{23}, $0 < \mu < 1$. The resulting sliding vector field is

$$S_{23}(x) = \frac{g(x)}{1 + kY} - bxY - \eta_2 x - (1 - \mu)(\eta_1 - \eta_2)x. \tag{4.21}$$

Equivalently,

$$S_{23}(x) = \frac{g(x)}{1 + kY} - bxY - \eta_1 x + \mu(\eta_1 - \eta_2)x. \tag{4.22}$$

After multiplying by the positive factor $(1 + kY)(x + n_0)/x$, the equation $S_{23}(x) = 0$ becomes

$$C_2 x^2 + C_1 x + C_0 = 0, \tag{4.23}$$

with

$$\begin{aligned} C_2 &= -\frac{r}{K} + D, \\ C_1 &= \frac{r(K+m_0)}{K} + D(n_0 - x_2) - (1+kY)(bY+\eta_1), \\ C_0 &= -rm_0 - (1+kY)(bY+\eta_1)n_0 - Dn_0x_2, \end{aligned} \tag{4.24}$$

and

$$D = \frac{(1+kY)(\eta_1-\eta_2)aY}{\theta_1}. \tag{4.25}$$

The constant coefficient can be simplified as

$$C_0 = -rm_0 - (1+kY)n_0\left[bY + \eta_2 + \frac{d(\eta_1-\eta_2)Y}{\theta_1}\right] < 0 \tag{4.26}$$

because every factor in the bracket is positive. Hence $C_0 < 0$ follows from the parameter signs and is not an additional modeling restriction. The sign of C_2 is

$$C_2 > 0 \quad \Longleftrightarrow \quad aY(1+kY)K(\eta_1-\eta_2) > r\theta_1. \tag{4.27}$$

A parameter condition sufficient for every $k \geq 0$ is

$$aYK(\eta_1-\eta_2) > r\theta_1. \tag{4.28}$$

For the baseline parameters, $aYK(\eta_1-\eta_2) = 1.368$ and $r\theta_1 = 0.30$, so (4.28) holds.

Proposition 4.1 (Endpoint interval for P_{23})**.** *Assume $x_2 \geq x_T$, $d/a < K$, the coefficient condition (4.28) holds, and $0 \leq k_L < k_R$. Let $I_{23} = (x_2, d/a)$; under these hypotheses, $x_L = x_2$, so $I_{23} = (x_L, d/a) \cap (x_T, K)$ coincides with $(x_2, d/a)$. Suppose*

$$S_{23}(x_2; k_L) = 0, \qquad S_{23}(d/a; k_R) = 0.$$

Then, for every $k \in (k_L, k_R)$, the equation $S_{23}(x) = 0$ has exactly one root $x_{p23} \in I_{23}$, and

$$S'_{23}(x_{p23}) > 0, \qquad \frac{\mathrm{d}x_{p23}}{\mathrm{d}k} > 0.$$

At $k = k_L$, the root lies at the left endpoint $x = x_2$, and at $k = k_R$, it lies at the right endpoint $x = d/a$; these endpoints are not elements of the open sliding interval I_{23}.

Proof. Condition (4.28) gives $C_2 > 0$, and (4.26) gives $C_0 < 0$. The quadratic (4.23) therefore has one positive and one negative root. Then

$$\frac{\partial S_{23}}{\partial k}(x;k) = -\frac{Yg(x)}{(1+kY)^2} < 0$$

for $x \in [x_2, d/a]$ because $m_0 < x_T \leq x_2 < d/a < K$ makes $g(x) > 0$ on this interval. The sliding field is therefore strictly decreasing in k, and for $k \in (k_L, k_R)$,

$$S_{23}(x_2; k) < S_{23}(x_2; k_L) = 0,$$

$$S_{23}(d/a;k) > S_{23}(d/a;k_R) = 0.$$

The intermediate value theorem gives a root in $(x_2, d/a)$, and the root signs of the quadratic make this positive root unique. The polynomial $Q_{23}(x;k) = C_2x^2 + C_1x + C_0$ and $S_{23}(x)$ differ by the positive factor $(1 + kY)(x + n_0)/x$ for $x > 0$, so Q'_{23} and S'_{23} have the same sign at a root. Since $C_2 > 0$, the positive root satisfies $Q'_{23}(x_{p23}) > 0$, and so $S'_{23}(x_{p23}) > 0$. Differentiating $S_{23}(x(k), k) = 0$ gives

$$\frac{\mathrm{d}x_{p23}}{\mathrm{d}k} = -\frac{\partial S_{23}/\partial k}{\partial S_{23}/\partial x}.$$

Here

$$\frac{\partial S_{23}}{\partial k} = -\frac{Yg(x)}{(1+kY)^2} < 0, \qquad \frac{\partial S_{23}}{\partial x} = S'_{23}(x_{p23}) > 0,$$

and so $\mathrm{d}x_{p23}/\mathrm{d}k > 0$. The endpoint statements follow from the definitions of k_L and k_R. □

We write $P_{23} = (x_{p23}, y_T)$ for an interior pseudo-equilibrium on Σ_{23}.

Corollary 4.1 (Baseline Σ_{23} branch)**.** *For the baseline parameters, $x_2 = 1.200658 > x_T = 1.2$ and condition (4.28) holds. The two endpoint values are*

$$k_L = k_{23}^{\text{left}} \approx 0.043563, \qquad k_R = k_c \approx 0.067589.$$

At $k = k_L$, P_{23} starts at $x = x_2$. It remains inside I_{23} for $k_L < k < k_R$ and reaches $x = d/a$ at k_R. For $k > k_c$, the positive root lies outside the open interval, so no interior P_{23} remains on Σ_{23}.

At $k = 0.05$, the interior root is

$$x_{p23} \approx 1.21515, \qquad S'_{23}(x_{p23}) \approx 2.3987 > 0. \tag{4.29}$$

Since $S'_{23} > 0$, P_{23} repels the sliding flow along Σ_{23}, while the adjacent fields point toward the manifold. It is transversely attracting but unstable as a Filippov pseudo-equilibrium. When P_{12} is admissible, by contrast, $S'_{12} < 0$ makes it locally attracting on its sliding interval.

For the baseline case $x_2 \geq x_T$, the left endpoint value is

$$k_{23}^{\text{left}} = \frac{1}{Y}\left(\frac{g(x_2)}{x_2(bY+\eta_1)} - 1\right) \approx 0.043563. \tag{4.30}$$

At $x = d/a$, the identity

$$\frac{g(d/a)}{d/a} = (1 + ky_3^*)(by_3^* + \eta_2)$$

shows that $S_{23}(d/a) = 0$ exactly when $y_3^* = Y$, that is, at $k = k_c$. Proposition 4.1 and the endpoint identities above establish the existence interval and monotonic motion of P_{23}.

Table 5 reports the sliding lengths and pseudo-equilibrium coordinates at representative values of k, together with the transition events discussed in Section 5.

The roots y_1, y_2, y_3 inherit their monotonicity from N_1. For fixed $u \geq 0$, let $y_u(k)$ solve

$$\frac{g(x_T)}{1+ky} - bx_Ty - ux_T = 0.$$

The left-hand side is strictly decreasing in both k and y, so $y'_u(k) < 0$. It follows that y_1, y_2, y_3 all decrease with k.

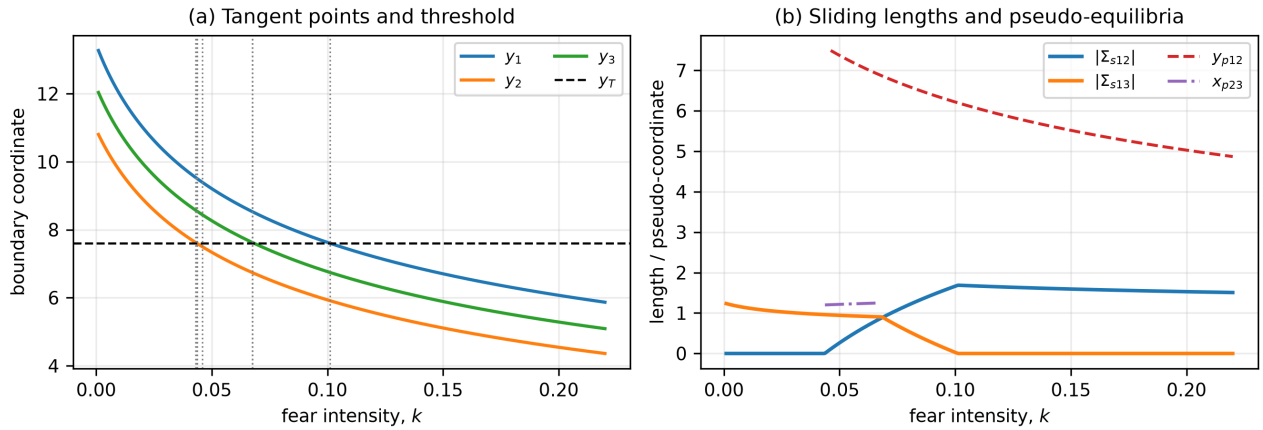


Figure 4. Fear dependence of the sliding geometry. (a) The tangent coordinates y_1, y_2, y_3 decrease with k. (b) Lengths of the vertical sliding intervals and the admissible pseudo-coordinates. The Σ_{23} pseudo-equilibrium is an interior point of the sliding interval only between k_{23}^{left} and k_c.

5. Threshold transitions

5.1. *Monotonicity of the high-enemy equilibrium*

At $E_3^* = (x^*, y_3^*)$,

$$(1 + ky_3^*)(by_3^* + \eta_2) = A_0. \tag{5.1}$$

Proposition 3.2(iv) implies that y_3^* and the fear load $L_3^* = ky_3^*/(1 + ky_3^*)$ vary monotonically with k.

The regular-to-virtual transition occurs when $y_3^* = y_T$. Substituting into (5.1) gives

$$k_c = \frac{1}{y_T}\left[\frac{g(x^*)}{x^*(by_T + \eta_2)} - 1\right]. \tag{5.2}$$

More generally,

$$k_c > 0 \iff A_0 > by_T + \eta_2 \iff y_3^*(0) > y_T.$$

The boundary interpretation below assumes $d/a > x_T$, so the positive F_3 equilibrium belongs to the closure of G_3. Under this condition, if $k_c > 0$, the equilibrium reaches Σ_{23} at a positive value of k. If $A_0 = by_T + \eta_2$, it already lies on Σ_{23} at $k = 0$. If $A_0 < by_T + \eta_2$, the smooth F_3 equilibrium is virtual for every $k \geq 0$. For the baseline,

$$k_c \approx 0.0676, \qquad E_3^*(k_c) \approx (1.25, 7.60). \tag{5.3}$$

If $A_0 > \eta_2$, then E_3^* is regular in G_3 for $0 < k < k_c$, lies on Σ_{23} at $k = k_c$, and is virtual for G_3 when $k > k_c$.

5.2. Transition order

The critical values are

$$\begin{aligned} k_{23}^{\text{left}} &\approx 0.043563, \\ k_{12}^{\text{act}} &\approx 0.043570, \\ k_{12}^{\text{lower}} &\approx 0.045926, \\ k_c &\approx 0.067589, \\ k_{13}^{\text{end}} &\approx 0.101185. \end{aligned} \tag{5.4}$$

Here

$$k_{12}^{\text{act}} : \ y_2(k) = y_T, \qquad k_{12}^{\text{lower}} : \ y_{p12}(k) = y_2(k),$$

and

$$k_{13}^{\text{end}} : \ y_1(k) = y_T.$$

The values satisfy

$$k_{23}^{\text{left}} < k_{12}^{\text{act}} < k_{12}^{\text{lower}} < k_c < k_{13}^{\text{end}}. \tag{5.5}$$

The first two critical values differ by only about 7.0×10^{-6}. We checked this near coincidence with one-percent changes in a, d, and x_T, one at a time. For each parameter set, we evaluated the horizontal entry value at $x_L = \max\{x_T, x_2\}$. When $x_L = x_2$, this value is k_{23}^{left}; when $x_L = x_T$, it solves $S_{23}(x_T; k) = 0$. Table 4 shows that three of the six perturbations reverse the baseline order and three keep it. The ordering is baseline-specific, not structurally universal.

Table 4. One-percent one-parameter sensitivity of the near-coincident transition thresholds. All other parameters remain at their baseline values. The horizontal entry value is evaluated at the actual left endpoint $x_L = \max\{x_T, x_2\}$; when $x_L = x_T$, it is obtained from $S_{23}(x_T; k) = 0$.

Perturbation	x_2	x_L	k_{23}^{entry}	k_{12}^{act}	Order
Baseline	1.200658	1.200658	0.043563	0.043570	$k_{23} < k_{12}$
$a \to 0.99a$	1.212786	1.212786	0.043428	0.043570	$k_{23} < k_{12}$
$a \to 1.01a$	1.188770	1.200000	0.048699	0.043570	$k_{23} > k_{12}$
$d \to 0.99d$	1.188158	1.200000	0.048932	0.043570	$k_{23} > k_{12}$
$d \to 1.01d$	1.213158	1.213158	0.043423	0.043570	$k_{23} < k_{12}$
$x_T \to 0.99x_T$	1.200658	1.200658	0.043563	0.043692	$k_{23} < k_{12}$
$x_T \to 1.01x_T$	1.200658	1.212000	0.048562	0.043437	$k_{23} > k_{12}$

The first ordering boundary is analytical. It occurs when $x_2 = x_T$, or equivalently, $y_T = \theta_1/(d - a\,x_T) = 7.5$. At this value, the left endpoint of I_{23} changes from x_2 to the corner x_T. The other two boundaries are numerical estimates. The ordering is specific to $y_T = 7.6$ and is not universal. The upper F_2 root enters G_2 at k_{23}^{left}, reaches Σ_{12} at k_{12}^{lower}, and is virtual outside this interval. To separate general structure from scenario-specific ordering, define the effective entry values

$$k_{12}^{\text{entry}} = \max\{k_{12}^{\text{lower}}, k_{12}^{Y}\}, \qquad k_{23}^{\text{entry}} = \max\{k_{23}^{\text{left}}, k_{23}^{x_T}, 0\}.$$

Here k_{12}^{Y} solves $y_{p12}(k) = y_T$, and $k_{23}^{x_T}$ solves $x_{p23}(k) = x_T$ when the root lies to the left of the corner. These adjustments are needed because a formal pseudo-equilibrium root is not an interior point of

the sliding interval when it lies outside the interval or above y_T. If $x_2 < x_T$, the left endpoint is the corner; $k_{23}^{x_T}$ denotes the positive solution of $S_{23}(x_T; k) = 0$ when it exists, and the effective value is $\max\{k_{23}^{\text{left}}, k_{23}^{x_T}, 0\}$.

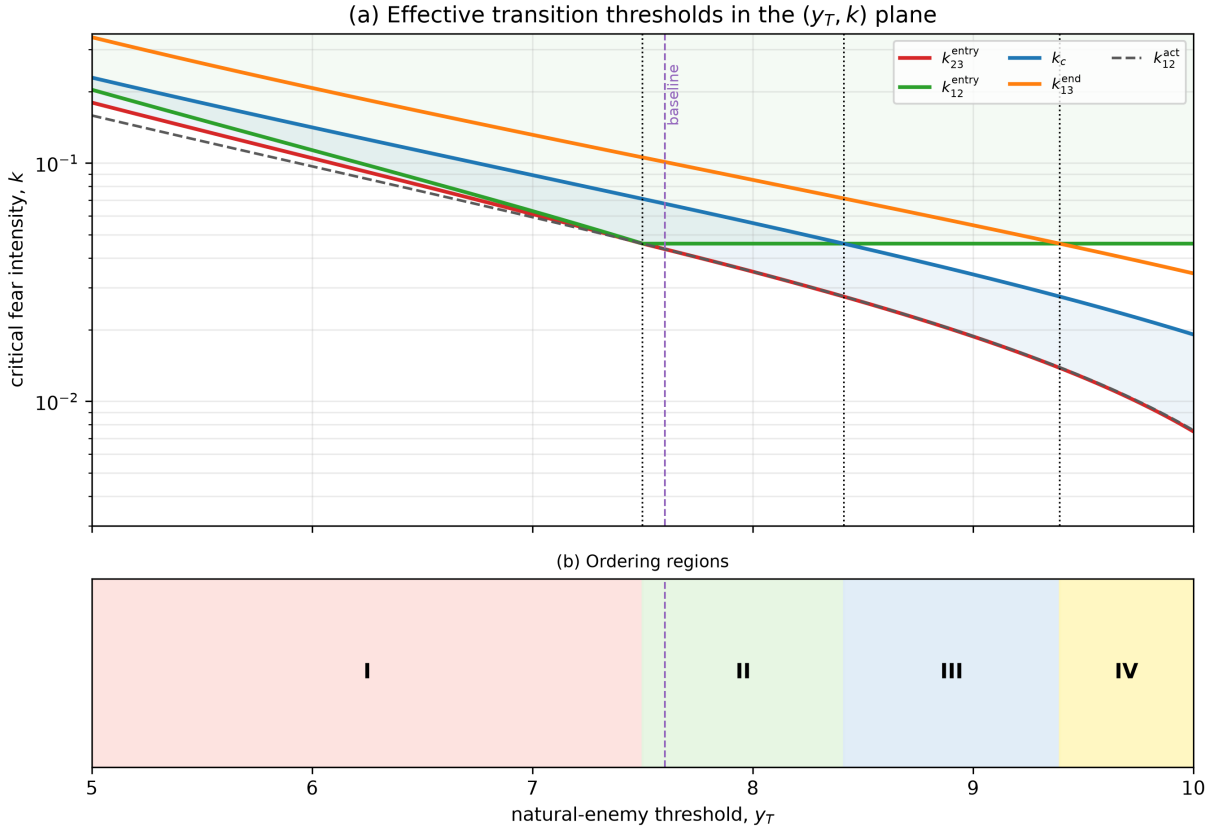


Figure 5. Numerically identified ordering regions for the baseline parameters and $5 \le y_T \le 10$. (a) Effective entry thresholds k_{12}^{entry}, k_{23}^{entry}, the boundary value k_c, the Σ_{13} endpoint k_{13}^{end}, and the sliding activation value k_{12}^{act}. The shaded band shows the interior interval of P_{23}. (b) The scan indicates four regions separated by $y_T \approx 7.5$, 8.412736, and 9.392716. The baseline is $y_T = 7.6$. The first boundary, $y_T = 7.5$, follows analytically from $x_2 = x_T$; the other two boundaries are numerical estimates.

Within the scanned interval, the effective thresholds divide the displayed y_T-range into four ordering regions (Figure 5(b)). For $5 < y_T < 7.5$, the order is $k_{12}^{\text{act}} < k_{23}^{\text{entry}} < k_{12}^{\text{entry}} < k_c < k_{13}^{\text{end}}$. Above $y_T \approx 7.5$, the first two values swap. Another ordering change occurs near $y_T = 8.412736$, where k_c crosses k_{12}^{entry}, and a third near $y_T = 9.392716$, where k_{13}^{end} falls below k_{12}^{entry}. These are numerical boundaries for the scanned interval, not an exhaustive bifurcation classification.

Table 5 lists the baseline sliding quantities and transition sequence. The upper F_2 root is regular in G_2 between k_{23}^{left} and k_{12}^{lower}. The Σ_{12} pseudo-equilibrium becomes locally attracting after it enters its sliding interval. The Σ_{23} pseudo-equilibrium is unstable and reaches $x = d/a$ at k_c, where it coincides with the boundary equilibrium E_3^*. For $k > k_c$, E_3^* is virtual for G_3 and the interior Σ_{23} pseudo-equilibrium is absent.

Table 5. Baseline sliding quantities and transition sequence versus the fear intensity k. The horizontal sliding length is constant, $|\Sigma_{s23}| = \theta_1/(ay_T) \approx 0.049342$; this formula uses the baseline condition $x_2 \geq x_T$, and in general the left endpoint of the sliding set is $x_L = \max\{x_T, x_2\}$, cf. (4.18). "boundary" marks a pseudo-equilibrium at an endpoint of its sliding interval and "–" an inadmissible one.

k	$\lvert\Sigma_{s12}\rvert$	$\lvert\Sigma_{s13}\rvert$	y_{p12}	x_{p23}	Event
0.020000	0.000000	1.055979	–	–	
0.043563	0.000000	0.960215	–	boundary	$S_{23}(x_2) = 0$: upper F_2 root meets (x_2, y_T)
0.043570	0.000000	0.960195	–	1.200674	$y_2 = y_T$: Σ_{12} enters $y < y_T$
0.045926	0.100000	0.953558	boundary	1.206098	$y_{p12} = y_2$: upper F_2 root reaches Σ_{12}
0.050000	0.263677	0.942872	7.368554	1.215149	baseline
0.067589	0.862335	0.905518	6.882090	boundary	$y_3^* = y_T$: P_{23} reaches $x = d/a$
0.080000	1.205557	0.541597	6.599287	–	
0.100000	1.663657	0.027131	6.217546	–	
0.101185	1.687862	0.000000	6.197242	–	$y_1 = y_T$: positive part of I_{13} disappears

5.3. *Endpoint collision on* Σ_{23}

At $k = k_c$, the event on Σ_{23} is a boundary-equilibrium/endpoint collision in the Filippov sense. The pseudo-equilibrium P_{23}, which exists only in the interior of I_{23}, reaches the right endpoint $x = d/a$ at the same parameter value at which the smooth equilibrium E_3^* reaches the switching manifold and becomes a boundary equilibrium. As k passes through k_c, E_3^* changes from regular in G_3 to virtual, and the interior Σ_{23} pseudo-equilibrium disappears. We do not assign a classical sliding-bifurcation name because the required transversality and nondegeneracy conditions have not been verified here. Figure 6 shows the endpoint collision. Panel (a) follows $x_{p23}(k)$ from the left endpoint to $x^* = d/a$. Panel (b) shows $y_3^*(k)$ reaching y_T. Panel (c) compares S_{23} at $k = 0.05$ and $k = k_c$; at k_c, the positive root reaches the right endpoint. The same left endpoint marks the start of the regular window of the upper F_2 equilibrium, which enters G_2 for $k > k_{23}^{\text{left}}$ and reaches Σ_{12} at k_{12}^{lower}.

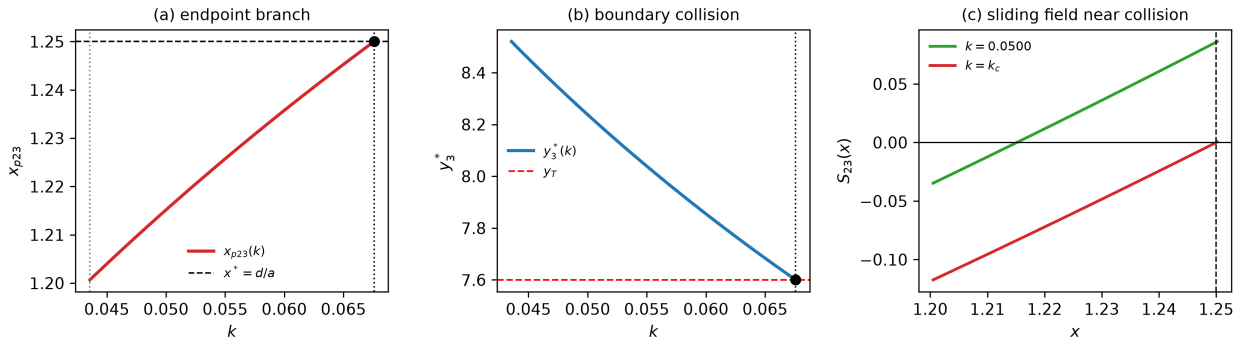


Figure 6. Endpoint collision on Σ_{23}.

5.4. *Numerical computation and finite-grid outcomes*

The numerical work uses two schemes. Grid sweeps use fixed-step projected RK4 with $\Delta t = 5\times10^{-3}$, or 2.5×10^{-3} in the step check. When a step crosses $x = x_T$ or $y = y_T$, the crossing coordinate is projected to the threshold and the active field is updated. No event-time bisection is used in these grid sweeps. Representative trajectories and event logs use MATLAB `ode45` with event functions and the scalar sliding flows. A separate event-localized RK4 routine with 60 bisections is used only for the single-trajectory check in Figure 7 and Table 6. Zero-normal contacts follow the derivative test in Appendix B; the corner follows Remark 2.2.

For the representative initial condition $(x_0, y_0) = (1, 8)$, the event-localized RK4 solution is compared with a high-accuracy MATLAB reference for the same pre-event and sliding equations. The reference uses `ode45` with RelTol $= 10^{-12}$ and AbsTol $= 10^{-14}$. Threshold values are computed from their defining equations, not estimated from this trajectory. Since both methods use the same switching and sliding formulation, the comparison tests numerical consistency rather than model validity. Figure 7 and Table 6 report the pre-event error at $t = 1$, the post-event errors at $t = 2$ and $t = 5$, and the first event-time error. The pre-event and $t = 5$ errors are of order 10^{-13}; the $t = 2$ and event-time errors are of order 10^{-12}. All four quantities are essentially independent of Δt over $5 \times 10^{-4} \le \Delta t \le 4 \times 10^{-3}$ because they are limited by the reference tolerance.

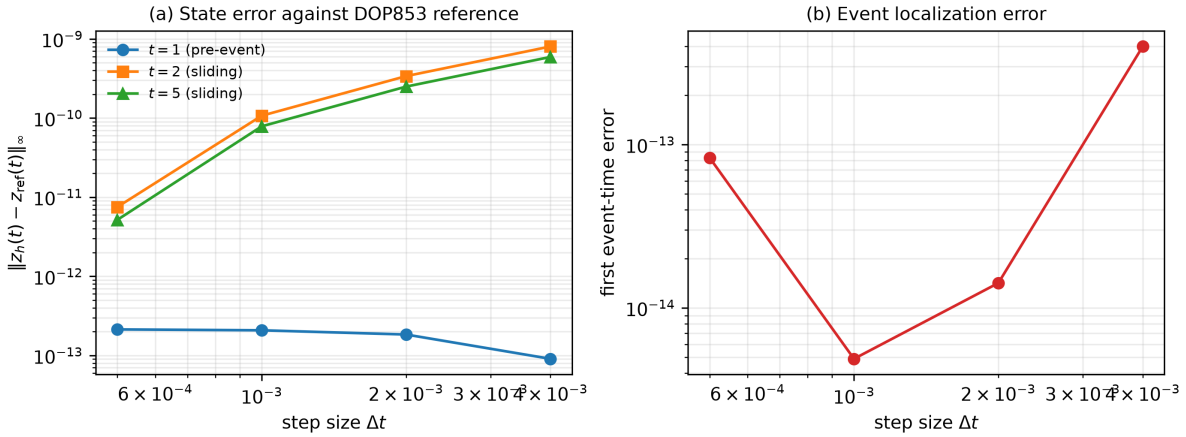


Figure 7. State and event-time errors against a high-accuracy MATLAB integration of the same equations.

Table 6. Event-localized RK4 against a high-accuracy MATLAB reference for $(x_0, y_0) = (1, 8)$. Errors are measured in the infinity norm; all four columns are limited by the tolerance of the reference solver.

Δt	Pre-event $t = 1$	$t = 2$	$t = 5$	Event time
4×10^{-3}	1.2×10^{-13}	1.3×10^{-12}	1.1×10^{-13}	1.9×10^{-12}
2×10^{-3}	3.9×10^{-13}	1.1×10^{-12}	2.5×10^{-13}	1.5×10^{-12}
10^{-3}	4.1×10^{-13}	1.1×10^{-12}	2.8×10^{-13}	1.5×10^{-12}
5×10^{-4}	4.0×10^{-13}	1.1×10^{-12}	2.9×10^{-13}	1.4×10^{-12}

A second representative trajectory, again from $(x_0, y_0) = (1, 8)$, at $k = 0.0435701465$ contains seven

events: one crossing of the vertical interface, sliding entry and exit on the horizontal interface, a switch to the upper region, sliding entry and exit on the vertical interface, and a final vertical crossing. Halving the step size from 2×10^{-3} to 10^{-3} preserves this event sequence; the maximum absolute event-time difference is 5.5×10^{-12}. The event sequence and times are included in the supplementary event log.

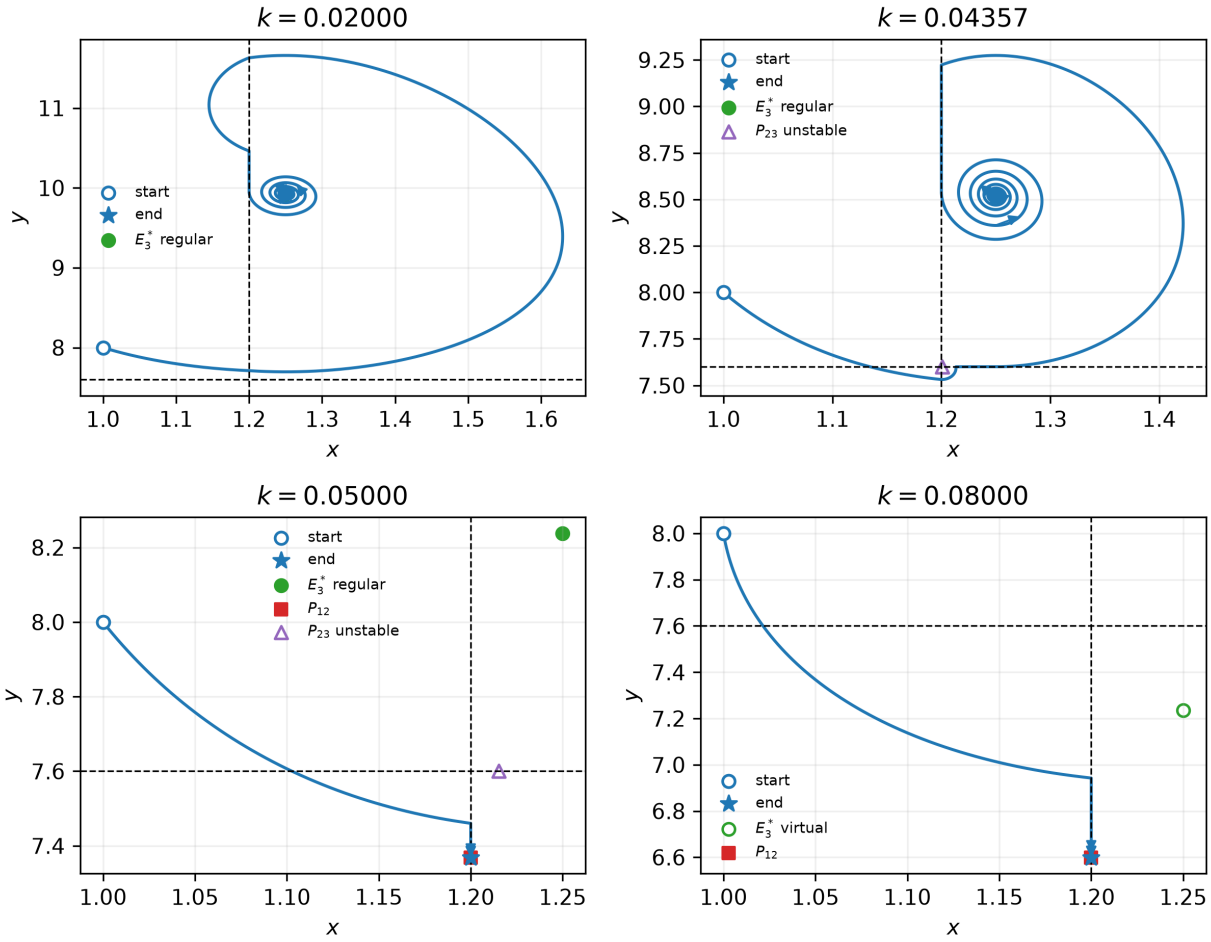


Figure 8. Representative trajectories from $(x_0, y_0) = (1, 8)$ over $0 \le t \le 100$. Time increases along each trajectory. Open circles mark the initial state, stars mark the terminal state, and arrows show the direction of motion. Filled equilibrium symbols denote regular states; open symbols denote virtual states. The threshold lines are $x = x_T$ and $y = y_T$. The panels show trajectories ending near E_3^* or the attracting Σ_{12} pseudo-equilibrium. When $k > k_c$, E_3^* is virtual and is shown only as a reference point.

At $k = 0.05$, both E_3^* and P_{12} are locally stable, and we record terminal states at $T = 100$. Near E_3^*, $\operatorname{tr} J \approx -0.079$ and $\det J \approx 0.440$, so the real parts of the eigenvalues are about -0.040 and the decay time is about 25 time units. On Σ_{12}, $S'_{12}(y_{p12}) < 0$, so attraction along the sliding manifold is exponential. The counts do not change for classification radii 0.04, 0.08, and 0.12, and the finest grid leaves no endpoint unresolved. Repeating the 40×40 diagnostic grid at $T = 200$ with the same step and rule leaves all 1600 labels unchanged; the counts are $(55, 1268, 277, 0)$ (Table 7). Once $x(T) < m_0$, $\dot{x} < 0$ in every active field, so a low-pest label cannot reverse. Near E_3^* and P_{12}, hyperbolicity gives exponential

contraction. On the 320×320 grid, the largest terminal distances from these states are below 0.024 and 7.4×10^{-5}; both lie well inside the 0.08 radius. A later relabeling would require leaving the local basin, not small numerical drift.

The 80×80, 160×160, and 320×320 grids test spatial resolution at $T = 100$. We call a state low-pest if $x(T) < m_0 = 0.10$. It is E_3^*-type if $x(T) > x_T$, $y(T) > y_T$, and $\|z(T) - E_3^*\| < 0.08$. It is P_{12}-type if $|x(T) - x_T| < 10^{-8}$, $y(T) < y_T$, and $\|z(T) - P_{12}\| < 0.08$. All other states are unresolved. Initial conditions are equally spaced on

$$0.15 \le x_0 \le 2.0, \qquad 0.4 \le y_0 \le 12.0.$$

Changing the classification radius does not affect the counts: radii 0.04, 0.08, and 0.12 give the same result. On the 320×320 grid, the largest distance among E_3^* assignments is below 0.024, the largest among P_{12} assignments is below 7.4×10^{-5}, and no endpoint is unresolved. For the 80×80, 160×160, and 320×320 grids, the low-pest, E_3^*, P_{12}, and unresolved counts are, respectively,

$$(191, 5096, 1113, 0), \quad (713, 20372, 4515, 0),$$
$$(2752, 81516, 18132, 0).$$

These are terminal-state counts inside the stated rectangle, not global basin areas. On the 40×40 validation grid, lowering Δt from 5×10^{-3} to 2.5×10^{-3} leaves every label unchanged (Table 7). None of the runs produced a nonfinite trajectory, an event-limit stop, a corner event, or a box exit.

Table 7. Step-size and label-stability diagnostics on the 40×40 validation grid, and an integration-horizon check at $T = 200$ with the same grid, step size, and classification criteria.

Δt	Low-pest	E_3^*	P_{12}	Unresolved	Nonfinite	Event-limit	Corner / Box exit
5×10^{-3}	55	1268	277	0	0	0	0 / 0
2.5×10^{-3}	55	1268	277	0	0	0	0 / 0
5×10^{-3}, $T = 200$	55	1268	277	0	0	0	0 / 0

5.5. Secondary numerical example

The baseline illustrates the local transitions but does not sample every nonsmooth geometry. We add a second dimensionless parameter set:

$$\begin{aligned}&(r, K, n_0, m_0, b, a, d)\\ &= (1.5, 4.5, 0.5, 0.1, 0.1, 0.5, 0.6),\\ &(\eta_1, \eta_2, \theta_1, x_T) = (0.3, 0.1, 0.1, 0.8).\end{aligned} \tag{5.6}$$

This set is an illustration, not a calibrated management scenario. We take

$$y_T \in \{3.5, 3.8, 3.84, 5.1\}, \qquad k \in \{0, 0.05\},$$

integrate each trajectory from $(0.45, y_T + 0.4)$ for 100 time units, and compute tail statistics over the last 40% of the run. The paths are shown in Figure 10, and Table 8 reports their tail extrema and event counts.

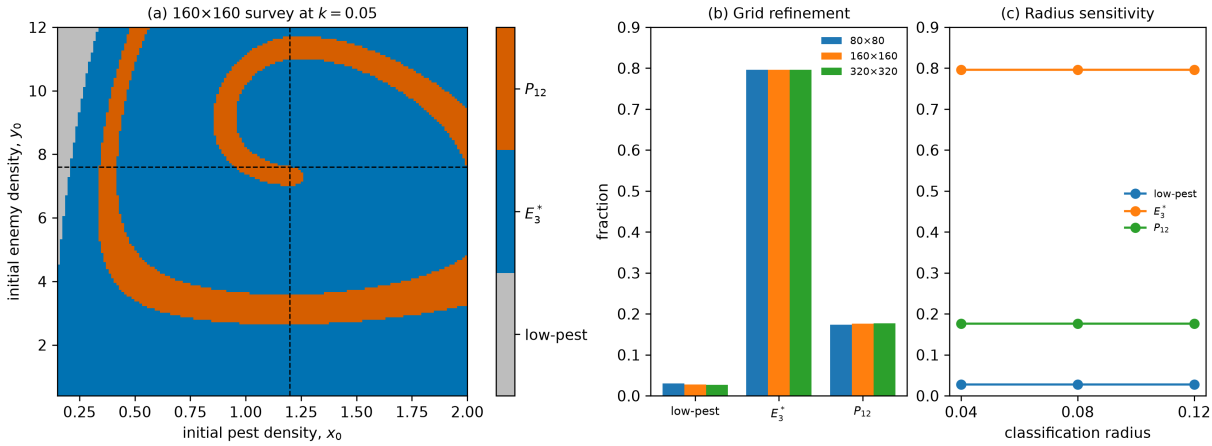


Figure 9. (a) Finite-grid outcome survey at $k = 0.05$ on a 160×160 grid. (b) Fractions on 80×80, 160×160, and 320×320 grids. (c) Sensitivity to the classification radius. The panel reports terminal-state categories under the rule in the text.

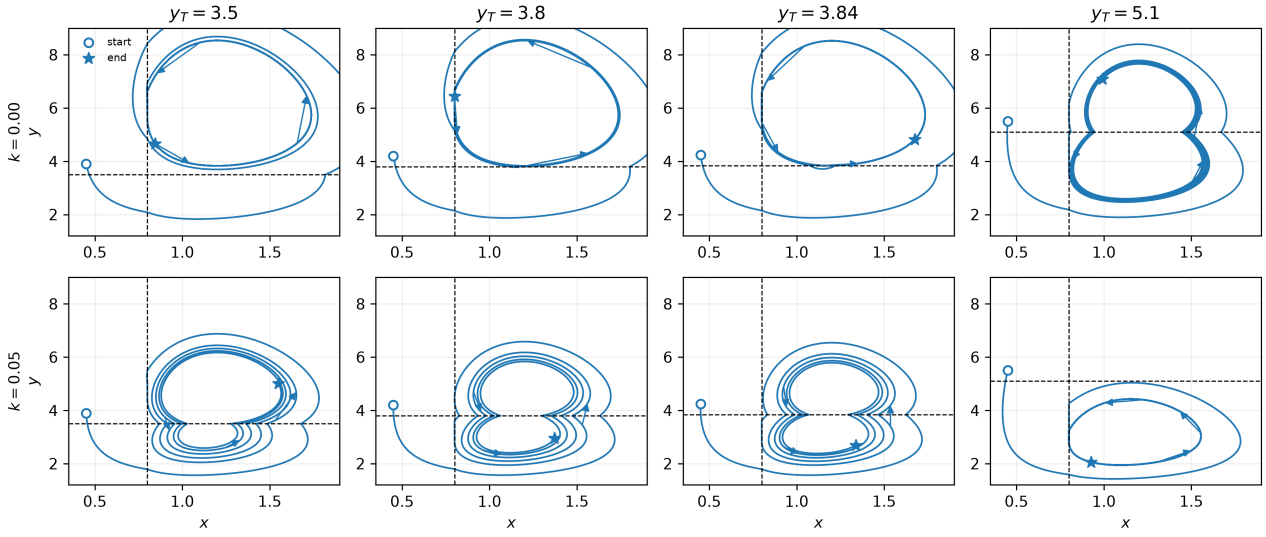


Figure 10. Trajectories in the secondary scenario over $0 \le t \le 100$. Top row: $k = 0$. Bottom row: $k = 0.05$. Columns: $y_T = 3.5, 3.8, 3.84, 5.1$. Time increases along each trajectory; open circles mark the initial state, stars mark the terminal state, and arrows show the direction of motion. Dashed lines mark the switching thresholds. Periodic orbits are not classified.

Table 8. Tail extrema and event counts for the trajectories in Figure 10. The tail is the last 40% of a 100-time-unit run. The event count includes crossing and sliding entry/exit events; no corner event occurred.

k	y_T	$x_{\min}$	$x_{\max}$	$y_{\min}$	$y_{\max}$	Events
0.00	3.50	0.8000	1.7376	3.8277	8.5372	29
0.00	3.80	0.8000	1.7376	3.8277	8.5372	30
0.00	3.84	0.8000	1.7342	3.8388	8.5238	55
0.00	5.10	0.8191	1.5727	2.5611	7.7216	18
0.05	3.50	0.8670	1.5925	2.4931	6.2345	16
0.05	3.80	0.9070	1.5034	2.3381	5.9170	17
0.05	3.84	0.9018	1.4895	2.3193	5.8665	14
0.05	5.10	0.8000	1.5554	1.9437	4.4286	22

For this initial condition, larger k lowers $x_{\max}$, $y_{\max}$, and the y-range in all four runs. The x-range shrinks for $y_T = 3.5, 3.8, 3.84$, but changes slightly from 0.7536 to 0.7554 at $y_T = 5.1$. The paths visit several regions and contain crossings and sliding episodes. These integrations are illustrative; periodic orbits are not classified here.

6. Discussion

The trace identity is the algebraic center of the G_1/G_3 analysis. At E_1^* and E_3^*, the trace is $\psi(x^*)/[x^*(1+ky^*)]$. The denominator is positive. If $\psi(x^*) \neq 0$, no value of k can move the trace through zero. At the baseline, $\psi(x^*) < 0$, so both regular coexistence states are stable. This is a local statement for smooth fields; virtual points and sliding intervals are separate.

In G_2, the scalar level function carries the main computational gain. It reduces existence, multiplicity, and the determinant sign to crossings of $L = 1$. A Sturm count then gives a reproducible root number at fixed coefficients, without a parameter-by-parameter bifurcation scan. The terminal threshold satisfies $\max_x L(x; k_*) = 1$, and a tangency occurs there. Baseline tracking finds one critical branch; this is not a general uniqueness proof. The upper branch is regular and stable only between k_{23}^{left} and k_{12}^{lower}; at $k = 0.05$, it is already virtual in F_2.

The two-threshold architecture is not new. What is new here is following k through both the equilibrium and sliding problems, using a fear-dependent trace identity, the scalar reduction $L = 1$, and a conditional endpoint relation. For $d/a > x_T$, E_3^* meets $y = y_T$ at k_c and becomes virtual beyond it. At the same value, P_{23} reaches $x = d/a$ and collides with that boundary point. The horizontal point attracts across the manifold but is unstable along the sliding flow. Finite runs end near Σ_{12} or E_3^*.

One might expect stronger fear to destabilize coexistence. In G_1 and G_3, it does not: the enemy ordinate drops while the trace sign stays fixed. The stronger effect appears in G_2, where fear can eliminate the release-and-spray equilibrium and leave only a narrow regular window. At k_c, the reduced-dose equilibrium reaches the release threshold; beyond it, the finite-grid runs end at low pest or at the Σ_{12} pseudo-equilibrium. Below m_0, fear slows decline only because it multiplies the signed growth term. That low-density effect follows from the chosen closure and is not a modeling target. These are model implications, not management rules; field calibration, multi-parameter sensitivity, and a cost criterion would be needed before any prescription.

The results divide along a clear line. Trace factorization, determinant identity, and component counting use structural features. The uniqueness of x_M, the exact F_2 count, threshold order, pseudo-equilibrium direction, and the baseline stability mixture depend on parameters. We identify these as baseline-specific.

The numerical survey is deliberately narrow: one rectangle, one horizon, a linear functional response, one fear factor, and dimensionless parameters. The one-percent sensitivity check is local. The grid illustrates threshold outcomes; it does not estimate global basin areas.

Miao et al. [36] studied invariant tori in a quasi-periodically forced discontinuous oscillator. Duan et al. [37] developed symbolic dynamics for piecewise smooth maps. Duan et al. [38] analyzed strange nonchaotic attractors in forced piecewise smooth systems. Those settings are map-based or externally forced and do not imply the same behavior in the autonomous planar system studied here.

7. Conclusions

Fear does not act as a simple stabilizer. In G_1 and G_3 it lowers the enemy abundance at which coexistence is possible, yet $x = d/a$ and the trace sign remains fixed. In G_2 the effect is sharper: the release-and-spray equilibrium survives only in a narrow fear interval. At k_c, the reduced-dose equilibrium meets the boundary equilibrium, and the regular-to-virtual change of E_3^* is tied to the sliding endpoint.

The mathematical gain is the scalar structure: the trace factorization and L give reproducible local tests, while Sturm counting fixes the baseline root number and L' fixes the determinant sign. The finite-grid map separates low-pest, E_3^*, and P_{12} outcomes. Saturating predation, separate birth and death terms for fear, and return maps are natural next steps.

Use of Generative-AI tools declaration

The authors declare they have not used Artificial Intelligence (AI) tools in the creation of this article.

Data availability

No external empirical data sets were used in this study. The numerical output tables, representative event logs, larger basin matrices, and MATLAB implementation are supplied in the archive `supplementary_material.zip`. During peer review this archive is available through the journal's submission system; after acceptance, it will be published online as Supplementary Material with the article.

Conflict of interest

The authors declare that they have no relevant financial or non-financial interests to disclose.

References

1. A. F. Filippov, *Differential Equations with Discontinuous Righthand Sides*, Kluwer Academic Publishers, Dordrecht, 1988. https://doi.org/10.1007/978-94-015-7793-9

2. Y. A. Kuznetsov, S. Rinaldi, A. Gragnani, One-parameter bifurcations in planar Filippov systems, *Int. J. Bifurcation Chaos*, **13** (2003), 2157–2188. https://doi.org/10.1142/S0218127403007874

3. M. di Bernardo, C. J. Budd, A. R. Champneys, P. Kowalczyk, A. B. Nordmark, G. Olivar Tost, et al., Bifurcations in nonsmooth dynamical systems, *SIAM Rev.*, **50** (2008), 629–701. https://doi.org/10.1137/050625060

4. K. S. Andrade, O. M. L. Gomide, D. D. Novaes, Bifurcation diagrams of global connections in Filippov systems, *Nonlinear Anal. Hybrid Syst.*, **50** (2023), 101397. https://doi.org/10.1016/j.nahs.2023.101397

5. D. J. W. Simpson, The stability of boundary equilibria of three-dimensional Filippov systems, *Nonlinear Anal. Hybrid Syst.*, **62** (2026), 101785. https://doi.org/10.1016/j.nahs.2026.101785

6. S. Tang, J. Liang, Y. Xiao, R. A. Cheke, Sliding bifurcations of Filippov two-stage pest control models with economic thresholds, *SIAM J. Appl. Math.*, **72** (2012), 1061–1080. https://doi.org/10.1137/110847020

7. Y. Zhang, Y. Xiao, Global dynamics for a Filippov epidemic system with imperfect vaccination, *Nonlinear Anal. Hybrid Syst.*, **38** (2020), 100932. https://doi.org/10.1016/j.nahs.2020.100932

8. H. Wang, Y. Xiao, C. Xiang, S. R. Smith, Classification of planar Filippov systems with a delayed threshold: applications to infectious disease transmission dynamics, *Nonlinear Anal. Hybrid Syst.*, **61** (2026), 101711. https://doi.org/10.1016/j.nahs.2026.101711

9. S. Tang, Y. Xiao, L. Chen, R. A. Cheke, Integrated pest management models and their dynamical behaviour, *Bull. Math. Biol.*, **67** (2005), 115–135. https://doi.org/10.1016/j.bulm.2004.06.005

10. T. Zhao, Y. Xiao, R. J. Smith, Non-smooth plant disease models with economic thresholds, *Math. Biosci.*, **241** (2013), 34–48. https://doi.org/10.1016/j.mbs.2012.09.005

11. B. Kang, X. Hou, B. Liu, Threshold control strategy for a Filippov model with group defense of pests and a constant-rate release of natural enemies, *Math. Biosci. Eng.*, **20** (2023), 12076–12092. https://doi.org/10.3934/mbe.2023537

12. W. Li, Y. Chen, L. Huang, J. Wang, Global dynamics of a Filippov predator–prey model with two thresholds for integrated pest management, *Chaos Solitons Fractals*, **157** (2022), 111881. https://doi.org/10.1016/j.chaos.2022.111881

13. L. Y. Zanette, A. F. White, M. C. Allen, M. Clinchy, Perceived predation risk reduces the number of offspring songbirds produce per year, *Science*, **334** (2011), 1398–1401. https://doi.org/10.1126/science.1210908

14. X. Wang, L. Zanette, X. Zou, Modelling the fear effect in predator–prey interactions, *J. Math. Biol.*, **73** (2016), 1179–1204. https://doi.org/10.1007/s00285-016-0989-1

15. M. Hu, C. Xiang, B. Chu, Dynamic behaviors and bifurcation analysis of a three-dimensional Filippov ecosystem with fear effect, *Math. Methods Appl. Sci.*, **48** (2025), 6607–6623. https://doi.org/10.1002/mma.10699

16. P. Panday, N. Pal, S. Samanta, J. Chattopadhyay, Stability and bifurcation analysis of a three-species food chain model with fear, *Int. J. Bifurcation Chaos*, **28** (2018), 1850009. https://doi.org/10.1142/S0218127418500098

17. A. Janssen, P. C. J. van Rijn, Pesticides do not significantly reduce arthropod pest densities in the presence of natural enemies, *Ecol. Lett.*, **24** (2021), 2010–2024. https://doi.org/10.1111/ele.13819

18. F. Wang, R. Yang, X. Zhang, Turing patterns in a predator–prey model with double Allee effect, *Math. Comput. Simul.*, **220** (2024), 170–191. https://doi.org/10.1016/j.matcom.2024.01.015

19. X. Kong, R. Yang, Dynamics analysis of a Filippov *Lymantria dispar*–Great tit model with double Allee effects and two-thresholds control, *Math. Comput. Simul.*, **246** (2026), 25–43. https://doi.org/10.1016/j.matcom.2026.01.028

20. A. M. Liebhold, P. C. Tobin, Population ecology of insect invasions and their management, *Annu. Rev. Entomol.*, **53** (2008), 387–408. https://doi.org/10.1146/annurev.ento.52.110405.091401

21. P. C. Tobin, L. Berec, A. M. Liebhold, Exploiting Allee effects for managing biological invasions, *Ecol. Lett.*, **14** (2011), 615–624. https://doi.org/10.1111/j.1461-0248.2011.01614.x

22. J. L. Rocha, A. K. Taha, D. Fournier-Prunaret, Transcritical and Neimark–Sacker bifurcations of a discrete predator–prey model of γ-Ricker type with double Allee effect in the prey population, *Commun. Nonlinear Sci. Numer. Simul.*, **154** (2026), 109543. https://doi.org/10.1016/j.cnsns.2025.109543

23. D. S. Boukal, L. Berec, Single-species models of the Allee effect: extinction boundaries, sex ratios and mate encounters, *J. Theor. Biol.*, **218** (2002), 375–394. https://doi.org/10.1006/jtbi.2002.3084

24. J. L. Rocha, D. Fournier-Prunaret, A. K. Taha, Strong and weak Allee effects and chaotic dynamics in Richards' growths, *Discrete Contin. Dyn. Syst. Ser. B*, **18** (2013), 2397–2425. https://doi.org/10.3934/dcdsb.2013.18.2397

25. A. A. Arafa, S. A. A. Hamdallah, S. Tang, Y. Xu, G. M. Mahmoud, Dynamics analysis of a Filippov pest control model with time delay, *Commun. Nonlinear Sci. Numer. Simul.*, **101** (2021), 105865. https://doi.org/10.1016/j.cnsns.2021.105865

26. H. Wang, Y. Yang, Dynamics analysis of a non-smooth Filippov pest–natural enemy system with time delay, *Nonlinear Dyn.*, **111** (2023), 9681–9698. https://doi.org/10.1007/s11071-023-08332-x

27. Y. Liu, Y. Yang, Dynamics and bifurcation analysis of a delay non-smooth Filippov Leslie–Gower prey–predator model, *Nonlinear Dyn.*, **111** (2023), 18541–18557. https://doi.org/10.1007/s11071-023-08789-w

28. X. Zhang, S. Tang, Existence of multiple sliding segments and bifurcation analysis of Filippov prey–predator model, *Appl. Math. Comput.*, **239** (2014), 265–284. https://doi.org/10.1016/j.amc.2014.04.098

29. W. Li, Bifurcation analysis of a Filippov predator–prey model with two thresholds, *Nonlinear Dyn.*, **112** (2024), 9639–9656. https://doi.org/10.1007/s11071-024-09527-6

30. S. A. A. Hamdallah, A. A. Arafa, Stability analysis of Filippov prey–predator model with fear effect and prey refuge, *J. Appl. Math. Comput.*, **70** (2024), 73–102. https://doi.org/10.1007/s12190-023-01934-z

31. W. Sun, Z. Xiang, Dynamical analysis of a Filippov pest–natural enemy model incorporating fear and prey refuge, *Electron. Res. Arch.*, **34** (2026), 7362–7391. https://doi.org/10.3934/era.2026318

32. L. Huang, W. Qin, S. Chen, Non-smooth dynamics of a Filippov predator–prey ecological model with antipredator behavior, *Adv. Contin. Discrete Models*, **2024** (2024), 13. https://doi.org/10.1186/s13662-024-03808-5

33. X. Jiao, L. Liu, X. Yu, Rich dynamics of a reaction–diffusion Filippov Leslie–Gower predator–prey model with time delay and discontinuous harvesting, *Math. Comput. Simul.*, **228** (2025), 339–361. https://doi.org/10.1016/j.matcom.2024.09.022

34. J. Lv, J. Li, The delayed reaction–diffusion Filippov system with threshold control: modeling and analysis of plateau pika–vegetation dynamics, *Commun. Nonlinear Sci. Numer. Simul.*, **152** (2026), 109366. https://doi.org/10.1016/j.cnsns.2025.109366

35. Z. Zhang, R. Yang, Dynamical analysis of a reaction–diffusion Filippov food chain model with threshold control, *Physica D*, **496** (2026), 135325. https://doi.org/10.1016/j.physd.2026.135325

36. P. Miao, J. Duan, D. Li, J. Xie, C. Grebogi, Existence and destruction of tori in a discontinuous oscillator under quasi-periodic excitations, *Physica D*, **481** (2025), 134804. https://doi.org/10.1016/j.physd.2025.134804

37. J. Duan, Z. Wei, D. Li, H. Su, C. Grebogi, Symbolic dynamics for a kinds of piecewise smooth maps, *Discrete Contin. Dyn. Syst. Ser. S*, **17** (2024), 2778–2787. https://doi.org/10.3934/dcdss.2024042

38. J. Duan, Z. Wei, G. Li, D. Li, C. Grebogi, Strange nonchaotic attractors in a class of quasiperiodically forced piecewise smooth systems, *Nonlinear Dyn.*, **112** (2024), 12565–12577. https://doi.org/10.1007/s11071-024-09678-6

Appendix A. Numerical verification

We recomputed the analytical quantities in the main text from their defining equations. Table A1 reports baseline residuals and derived checks for the equilibrium and sliding equations.

Table A1. Verification of baseline analytical quantities.

Quantity	Value	Check
x^*	1.250000000	d/a
$y_3^*(0.05)$	8.237973571	residual $< 10^{-13}$
$y_3^{*\prime}(0.05)$	−41.43656	derivative formula
$L_{xx}(x_f, k_*)$	−7.60086	baseline fold check
$L_k(x_f, k_*)$	−0.133339	baseline fold check
$\mathrm{tr}\, J_3(0.05)$	−0.079023795	stable focus, det = 0.440237476
$y_1(0.05)$	9.206480388	residual $< 10^{-13}$
$y_2(0.05)$	7.336322630	residual $< 10^{-13}$
$E_2^+(k_{23}^{\mathrm{left}})$	(1.200657895, 7.600000000)	on Σ_{23}
$E_2^+(k_{12}^{\mathrm{lower}})$	(1.200000000, 7.500000000)	on Σ_{12}
$y_{p12}(0.05)$	7.368553960	residual $< 10^{-13}$
$x_{p23}(0.05)$	1.215149241	$S'_{23}(x_{p23}) = 2.398659404 > 0$
k_{23}^{left}	0.0435631451	$S_{23}(x_2; k) = 0$
k_{12}^{act}	0.0435701465	$y_2(k) = y_T$
k_{12}^{lower}	0.0459259259	$y_{p12}(k) = y_2(k)$
k_c	0.0675893153	$y_3^*(k) = y_T$, $x_{p23}(k) = d/a$
k_{13}^{end}	0.1011849800	$y_1(k) = y_T$

The fold quantities in Table A1 were recomputed from (3.18) and (3.21). The comparison with a high-accuracy MATLAB reference is reported in Section 5.4 (Figure 7 and Table 6); it includes pre-event state errors, post-event state errors, and the first event-time error.

A.1. Sturm root count for the baseline F_2 polynomial

For fixed $k > 0$, let $Q_2(x; k)$ be defined by (3.19). Since $K(x + n_0)/x > 0$ on $(m_0, d/a)$, the zeros of $Q_2(\cdot; k)$ in this interval are exactly the positive equilibria of F_2. At the baseline parameters and $k = 0.05$,

$$\begin{aligned} Q_2(x; 0.05) = & -\frac{8}{25}x^4 + \frac{266}{125}x^3 - \frac{39{,}829}{10{,}000}x^2 \\ & + \frac{251{,}951}{100{,}000}x - \frac{150{,}867}{500{,}000}. \end{aligned} \tag{A.1}$$

Multiplying $Q_2(\cdot; 0.05)$ by the negative constant -5×10^5 gives an integer polynomial p_0 with the same zeros. The standard Sturm recursion $p_{i+1} = -\operatorname{rem}(p_{i-1}, p_i)$, with positive scaling at each step, gives

$$\begin{aligned} p_0 &= 160{,}000x^4 - 1{,}064{,}000x^3 + 1{,}991{,}450x^2 \\ &\quad - 1{,}259{,}755x + 150{,}867, \\ p_1 &= 640{,}000x^3 - 3{,}192{,}000x^2 + 3{,}982{,}900x - 1{,}259{,}755, \\ p_2 &= 4{,}236{,}160x^2 - 9{,}095{,}380x + 4{,}770{,}799, \\ p_3 &= 101{,}655{,}168{,}980x - 124{,}898{,}391{,}751, \\ p_4 &= 1. \end{aligned} \tag{A.2}$$

Positive scaling leaves the number of sign variations unchanged. The endpoint sign patterns are $(+, -, +, -, +)$ at $x = m_0$ and $(+, -, +, +, +)$ at $x = d/a$, which give four and two variations, respectively. Table A2 reports these values and the resulting root count. The sequence follows from exact polynomial remainder recursion and can be reproduced by a computer-algebra system or by hand. Neither endpoint

Table A2. Sturm root count for the baseline F_2 polynomial.

Endpoint	$V(x)$	Sign of $Q_2(x; 0.05)$	Root count
$m_0 = 0.1$	4	negative	–
$d/a = 1.25$	2	negative	$V(m_0) - V(d/a) = 2$

is a zero of $Q_2(\cdot; 0.05)$. Sturm's theorem gives exactly two distinct zeros in $(m_0, d/a)$, numerically, $x \approx 0.154414$ and $x \approx 1.198888$. At the lower root, $L' > 0$, so it is a saddle. At the upper root, $L' < 0$ and $T_2 < 0$, so it is a locally asymptotically stable focus of the extended F_2 field.

Appendix B. Numerical implementation and reproducibility

Grid sweeps use fixed-step projected RK4 with $\Delta t = 5 \times 10^{-3}$, or 2.5×10^{-3} for the step check. If a step crosses $x = x_T$ or $y = y_T$, the crossing coordinate is projected to the threshold and the active field is updated; no event-time bisection is used. Sliding segments use the same fixed step, with endpoint crossings projected onto the switching boundary. Representative trajectories and event logs

use MATLAB `ode45` event functions. The solver-consistency check uses a separate event-localized RK4 routine with 60 bisection iterations. At C, the restart rule in Remark 2.2 applies.

At a zero-normal contact $F_i^n = 0$, the code evaluates the signed switching coordinate $h(t)$ and its first nonzero derivative along the orbit. An even order keeps the orbit on the same side; an odd order crosses the manifold. If the one-sided normals satisfy the sliding inequalities, the contact is logged as a sliding boundary. At a sliding endpoint, let s parameterize the sliding interval and let $S(s)$ be the scalar sliding vector. If $S(s_e)$ points into the interval, the trajectory continues sliding. If it points out, the trajectory leaves along the adjacent field whose normal component points into its active side. None of the reported trajectories or grids hit an exact zero-normal contact; the derivative test is included for completeness. Event logs record the event type, time, segment, normals, derivative order, and chosen outgoing region. The workflow uses MATLAB R2019b or later and no toolboxes. Equilibrium branches, tangent roots, pseudo-equilibrium roots, the level function L, the transition map, and the endpoint collision come directly from the formulas in Sections 3–5. Grid calculations use fixed-step projected RK4 with $\Delta t = 5 \times 10^{-3}$ and $T = 100$. Event logs use `ode45` event functions, and the convergence check uses the separate event-localized RK4 routine.

The convergence study in Section 5.4 compares this scheme with a high-accuracy reference integration of the same equations using `ode45` at RelTol = 10^{-12} and AbsTol = 10^{-14}. The comparison is limited by the reference tolerance, so we infer no convergence order.

The two grid experiments answer different questions. The 40×40 diagnostic in Table 7 uses fixed-step projected RK4 at $\Delta t = 5 \times 10^{-3}$ and 2.5×10^{-3}; both give the same labels. A separate 40×40 demonstration uses the coarser step 10^{-2} and changes one boundary label. That run only shows the effect of an excessively large step and is not used for classification. Repeating the 40×40 fixed-step run at $T = 200$ leaves all 1600 labels unchanged. Event logs and numerical tables are supplied separately.

The MATLAB entry `run_table7` recomputes the $T = 100$ and $T = 200$ label matrices with $\Delta t = 5 \times 10^{-3}$ and writes `basin_diagnostics.json`. The entry `run_all` rebuilds all manuscript figures, including Figure 9, from the supplied 80×80, 160×160, and 320×320 matrices. Representative event logs contain `derivative_order` and `chosen_region`.



AIMS Press

© 2027 the Author(s), licensee AIMS Press. This is an open access article distributed under the terms of the Creative Commons Attribution License (https://creativecommons.org/licenses/by/4.0)